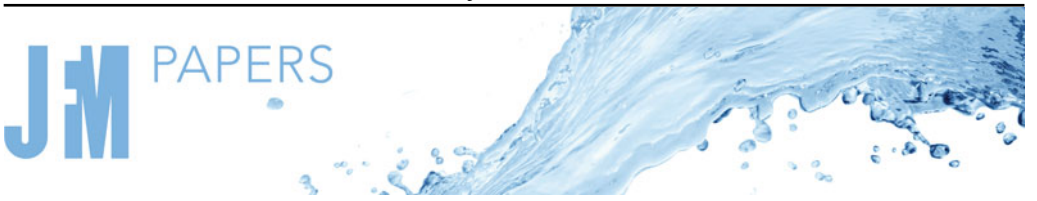
J. Fluid Mech. (2025), *vol.* 1025, A53, doi:10.1017/jfm.2025.10990



Electrically driven relaminarisation of particle-laden turbulent channel flow

Yuankai Cui[1,†], **Xuelian Tan**[1,†], **Huan Zhang**[1] and **Xiaojing Zheng**[2]

[1]Center for Particle-laden Turbulence, Lanzhou University, Lanzhou, Gansu 730000, PR China

[2]Research Center for Applied Mechanics, Xidian University, Xi'an 710071, PR China

Corresponding author: Huan Zhang, zhanghuan@lzu.edu.cn

(Received 6 July 2025; revised 28 September 2025; accepted 23 November 2025)

Electrical effects are known to play an important role in particle-laden flows, yet a holistic view of how they modulate turbulence remains elusive due to the complexity of multifield coupling. Here, we present a total of 119 direct numerical simulations of particle-laden turbulent channel flow that reveal a striking ability of electrical effects to induce turbulence relaminarisation and markedly alter wall drag. As expected, the transition from turbulence to laminar flow is accompanied by abrupt changes in the statistical properties of both the fluid and particulate phases. Nevertheless, with increasing electrical effects, the wall-normal profiles of the mean streamwise fluid velocity and mean local particle mass loading exhibit opposite trends in the turbulent and laminar regimes, arising from the competition between turbophoresis and electrostatic drift. We identify three distinct flow regimes resulting from the electrical effects: a drag-reduced turbulent regime, a drag-reduced laminar regime, and a drag-enhanced laminar regime. It is revealed that relaminarization originates from the complete suppression of the streak breakdown in the near-wall self-sustaining cycle, followed by the sequential inhibition of other subprocesses in the cycle. In the turbulent regime, increasing electrical effects induce opposing trends in Reynolds and particle stress contributions to drag, yielding a non-monotonic drag response. In laminar regimes, by contrast, the drag coefficient increases monotonically as the Reynolds stress vanishes and particle-induced stress becomes dominant.

Key words: particle/fluid flow

1. Introduction

Particle electrification is ubiquitous in particle-laden turbulent flows across diverse contexts, including natural phenomena, industrial applications, and even extraterrestrial

[†]These authors contributed equally to this work and should be considered co-first authors.

© The Author(s), 2025. Published by Cambridge University Press.

https://doi.org/10.1017/jfm.2025.10990 Published online by Cambridge University Press

environments. Examples encompass dust storms (Rudge 1913; Cranfield 1929; Harris 1967; Kamra 1972; Shinbrot & Herrmann 2008; Zhang & Zhou 2023), wind-blown sand (or sand saltation) (Schmidt, Schmidt & Dent 1998; Zheng, Huang & Zhou 2003; Kok & Renno 2008), dust devils (Freier 1960; Crozier 1964), blowing snow (Schmidt *et al.* 1999) and volcanic eruptions (Gilbert *et al.* 1991; Houghton, Aplin & Nicoll 2013; Cimarelli *et al.* 2014) in natural phenomena, and pneumatic conveying (Owen 1969) and fluidised beds (Sippola *et al.* 2018) in industrial applications, as well as dust activity on Mars (Farrell *et al.* 1999; Harrison *et al.* 2016) and on Titan, Saturn's largest moon (Méndez Harper *et al.* 2017), in extraterrestrial environments.

Historical accounts of electrical phenomena in particle-laden flows can be traced back to the 1850s, most notably in a letter from Michael Faraday: 'The quantity of Electricity which you obtain at the time is enormous ... That it (electricity) accompanies them (dust storms), there is no doubt of, but then, that may be as much in the way of effect as cause' (Baddeley 1860). Numerous experiments have demonstrated that turbulence-driven segregation of oppositely charged particles of different sizes can generate electric fields with mean intensities reaching $\mathcal{O}(10^2)$ kV m^{-1}, resulting in electrostatic forces on the particles comparable in magnitude to their gravitational forces (e.g. Stow 1969; Zheng *et al.* 2003; Zheng 2013; Zhang & Zhou 2020). Furthermore, fluctuations of the electric field exhibit a strong correlation with the fluid velocity and particle dynamics. Field measurements of dust storm turbulence at Qingtu Lake Observation Array indicate that, compared with the wind velocity and dust concentration spectra, the electric field power spectrum in the outer region displays a $-5/3$ power-law scaling over a broader range of wavenumbers (Zhang & Zhou 2023). This scaling behaviour is attributed to the cascade of space-charge-density variance and the presence of stronger and more extensive second-order nonlinear phase coupling in the electric field (Zhang & Zheng 2025). Rahman, Saieed & Hickey (2023) replicated this $-5/3$ scaling of electric fields using wall-modelled large-eddy simulations of charged particle-laden Martian boundary layers, suggesting the potential universality of this phenomenon. In addition to the wind velocity field, very-large-scale motions are also present in the electric field and dust concentration fields, with comparable streamwise length scales (Zhang 2024). Additionally, the small-scale intermittency of the electric field is stronger than that of velocity fluctuations but weaker than that of dust concentration. Wavelet-based conditioning statistics demonstrated that such intermittency in multiple fields predominantly originates from the contributions of their coherent structures (Zhang, Tan & Zheng 2023).

In general, turbulence, particles and electric fields are strongly and nonlinearly coupled (Zhang & Zheng 2025), thereby making the electric field a key factor influencing particle lifting, aggregation, transport and gravitational settling. Under typical dust storm conditions, particle electrification can lead to a tenfold increase in particle concentration compared to the uncharged case (Esposito *et al.* 2016), and may even directly lift particles into the air (Kok & Renno 2006). In homogeneous isotropic turbulence, theoretical predictions (Alipchenkov, Zaichik & Petrov 2004), laboratory experiments (Lu *et al.* 2010) and numerical simulations (Boutsikakis, Fede & Simonin 2022; Ruan, Gorman & Ni 2024) consistently show that particle electrification suppresses both particle clustering and dispersion. In turbulent channel flows, particles carrying like charges exhibit enhanced migration towards the wall, indicative of intensified wall accumulation (Zhang, Cui & Zheng 2023; Ruan *et al.* 2025). In the context of aeolian saltation, positive charging of sand grains enhances the horizontal particle mass flux, whereas negative charging suppresses it (Zheng *et al.* 2003; Kok & Renno 2008). For particle fallout from volcanic plumes, electrical effects significantly modify ash dispersal and deposition by promoting particle aggregation, which enhances proximal fallout of fine ash and alters

https://doi.org/10.1017/jfm.2025.10990 Published online by Cambridge University Press

transport trajectories. These interactions lead to polymodal grain-size distributions and dust coatings on larger particles, reducing atmospheric residence time and reshaping ash cloud dynamics (Gilbert *et al.* 1991).

Despite extensive research over the past century, little is known about how electrical effects modulate turbulence and which physical mechanisms govern this process. A major challenge lies in accurately resolving turbulent velocity fields under strong multifield coupling, particularly in the near-wall region, both experimentally and numerically (Bec, Gustavsson & Mehlig 2024). As a result of these limitations, existing studies have primarily focused on particle dynamics (e.g. Zheng *et al.* 2003; Kok & Renno 2008; Zhang *et al.* 2023) and charging characteristics (Grosshans & Papalexandris 2017; Jantač & Grosshans 2024). Early studies on aeolian sand saltation, based on Reynolds-averaged Navier–Stokes simulations by Zheng and co-workers, demonstrated that the increased saltation flux and particle concentration associated with positively charged particles can substantially reduce the mean streamwise wind velocity and enhance the aerodynamic surface roughness (Zheng *et al.* 2003, 2006). Large-eddy simulations of pipe flow laden with charged monodisperse particles have shown that electrical effects intensify particle–fluid coupling, leading to increased mean velocity but reduced Reynolds stress in the near-wall region (Zhao *et al.* 2022). More recently, our direct numerical simulations (DNS) of turbulent channel flow laden with charged bidisperse particles have shown that, relative to uncharged cases, electrified particles more effectively extract momentum from the fluid and amplify particle-induced dissipation of turbulent kinetic energy, thereby further suppressing turbulence intensity (Cui, Zhang & Zheng 2024). To date, it is well established that electrical effects can exert a pronounced influence on turbulence modulation. Nevertheless, a comprehensive understanding of how electrical effects modulate turbulence, along with the physical mechanisms governing this process, remains elusive.

To resolve this issue, we systematically investigate the influence of electrical effects on turbulence using 119 DNS of particle-laden turbulent channel flow. The remainder of the paper is structured as follows. Section 2 outlines the numerical model, simulation set-up and statistical procedures. In § 3, we present a phase diagram of the 119 simulation cases in the parameter space defined by particle mass loading and the electrical Stokes number (as introduced in § 2), and demonstrate that inter-particle electrostatic interactions can induce flow relaminarisation and substantially modify wall drag. To elucidate the underlying mechanisms, we examine the effects of electrical interactions on the near-wall self-sustaining cycle, and decompose the wall drag into contributions from viscous, Reynolds and particle stresses. Finally, the main findings are summarised in § 4.

2. Methodology

The DNS are performed using an Euler–Lagrange point-particle framework, where the carrier fluid phase is governed by the Navier–Stokes and continuity equations

$$\frac{\partial \boldsymbol{u}}{\partial t} + (\boldsymbol{u}\cdot\boldsymbol{\nabla})\boldsymbol{u} = -\boldsymbol{\nabla} p + \nu\,\boldsymbol{\nabla}^2\boldsymbol{u} + \boldsymbol{f}, \tag{2.1}$$

$$\boldsymbol{\nabla}\cdot\boldsymbol{u} = 0. \tag{2.2}$$

Here, $\boldsymbol{u}$ and p are the velocity and pressure per fluid density, respectively, ν denotes the fluid kinematic viscosity, and $\boldsymbol{f}$ represents the feedback force per fluid density of the particulate phase on the fluid flow. The streamwise, wall-normal and spanwise velocities are denoted by u, v and w, respectively, with the corresponding coordinates given by x, y and z.

https://doi.org/10.1017/jfm.2025.10990 Published online by Cambridge University Press

Re_τ	$L_x \times L_y \times L_z$	$N_x \times N_y \times N_z$	Δx_g^+	Δy_g^+	Δz_g^+
180	$4\pi\delta \times 2\delta \times 2\pi\delta$	$384 \times 192 \times 256$	5.89	0.25–3.25	4.42

Table 1. The DNS grid parameters. Here, L_x, L_y and L_z denote the streamwise, wall-normal and spanwise extents of the computational domain, respectively; $\delta = 0.06$ m is the channel half-width; N_x, N_y and N_z are the numbers of grid points in each direction; and Δx_g^+, Δy_g^+ and Δz_g^+ represent grid spacings normalised by viscous length scale $\delta_\nu = \nu/u_\tau$.

We consider a particle-free turbulent channel flow driven by a uniform pressure gradient. The simulation is conducted at friction Reynolds number $Re_\tau \equiv u_\tau \delta/\nu = 180$ (corresponding to bulk Reynolds number $Re_b \equiv U_b\delta/\nu = 2857$), where $u_\tau \equiv (\nu(\mathrm{d}\langle u\rangle/\mathrm{d}y)_{y=0})^{1/2}$ and U_b are the friction and bulk velocities, respectively, and $\delta = 0.06$ m is the channel half-width. The angle brackets $\langle\cdot\rangle$ indicate averaging over time and the wall-parallel (x–z) plane.

The computational domain spans $4\pi\delta \times 2\delta \times 2\pi\delta$, discretised with grid points $384 \times 192 \times 256$, sufficient to capture the full range of turbulence scales. The key grid parameters are summarised in table 1. Periodic boundary conditions are imposed in the streamwise and spanwise directions, while no-slip conditions are applied at the top ($y = 2\delta$) and bottom ($y = 0$) walls. Equations (2.1) and (2.2) are solved using the canonical Navier–Stokes solver developed by (Costa 2018), which employs a fast Fourier transform (FFT) based pressure projection method (Kim & Moin 1985).

Once the particle-free flow attains its final statistically steady state, sub-Kolmogorov-sized particles are randomly introduced throughout the computational domain, with their initial velocities set to match the local fluid velocity at their respective positions. The dispersed particles are significantly smaller than the Kolmogorov length scale of the carrier fluid. This justifies the use of a point-particle model, in which each particle can be tracked individually in the Lagrangian framework (Balachandar & Eaton 2010). To isolate the effects of the electric field and particle inertia, gravitational settling is neglected (e.g. Boutsikakis *et al.* 2022; Motoori, Wong & Goto 2022; Cui *et al.* 2024; Ruan *et al.* 2024, 2025). Given the large particle-to-fluid density ratio $\rho_p/\rho_f \gg 1$, the dominant hydrodynamic force acting on the particles is the Stokes drag (Maxey & Riley 1983). Thus the dimensionless form of Newton's equation of motion is written as (Maxey & Riley 1983; Maxey 1987; Zhang *et al.* 2023; Xu, Xu & Xi 2024)

$$\frac{\mathrm{d}\boldsymbol{x}_p^+}{\mathrm{d}t^+} = \boldsymbol{u}_p^+, \tag{2.3}$$

$$\frac{\mathrm{d}\boldsymbol{u}_p^+}{\mathrm{d}t^+} = \frac{1}{St^+}\left[\zeta\left(\boldsymbol{u}_{f@p}^+ - \boldsymbol{u}_p^+\right) + \frac{St_{el}^2}{St^+}\boldsymbol{E}_{@p}^+\right], \tag{2.4}$$

where $\boldsymbol{x}_p^+$ and $\boldsymbol{u}_p^+$ denote the particle position and velocity, respectively, while $\boldsymbol{u}_{f@p}^+$ and $\boldsymbol{E}_{@p}^+$ represent the fluid velocity and electric field at the particle position. The drag coefficient is given by $\zeta = 1 + 0.15\,Re_p^{0.687}$, where $Re_p \equiv d_p\,|\boldsymbol{u}_{f@p} - \boldsymbol{u}_p|/\nu$ is the particle Reynolds number (Schiller & Naumann 1935), and d_p is the particle diameter. The superscript $+$ indicates quantities normalised with respect to the viscous scales of the fluid phase, including the friction velocity u_τ, the viscous length scale $\delta_\nu = \nu/u_\tau$, the viscous time scale $t_\nu = \nu/u_\tau^2$, and their derived quantities. The electric field is normalised by $6\pi q n_0 \delta_\nu/\varepsilon_0$, where q, n_0 and ε_0 are the electric charge of the particle, bulk mean

https://doi.org/10.1017/jfm.2025.10990 Published online by Cambridge University Press

particle number density, and the permittivity of the vacuum, respectively. Time integration of (2.3) and (2.4) is performed using a standard fourth-order Runge–Kutta scheme.

In (2.4), the aerodynamic and electrical Stokes numbers are defined as $St^+ = t_p/t_v$ and $St_{el} = t_p/t_{el}$, respectively, where $t_p = \rho_p d_p^2/(18\nu\rho_f)$ represents particle inertial response time (Eaton & Fessler 1994), and $t_{el} = (\rho_p \pi^2 \varepsilon_0 d_p^3/(n_0 q^2))^{1/2}$ characterises the time scale of inter-particle electrostatic interactions (Boutsikakis *et al.* 2022). Here, ρ_p and ρ_f denote the particle mass density and fluid mass density, respectively. By definition, the larger the aerodynamic (electrical) Stokes numbers, the greater the intensity of particle inertial (electrical) effects.

Of particular note is that $\boldsymbol{E}^+_{@p}$ is calculated using the particle–particle–particle–mesh method (e.g. Kolehmainen *et al.* 2016; Zhang *et al.* 2023; Cui *et al.* 2024), which accounts for both short- and long-range inter-particle electrostatic interactions. The dimensional electric field at a particle's location, $\boldsymbol{E}_{@p}$, consists of the long-range component $\boldsymbol{E}_{l@p}$, the short-range contribution $\boldsymbol{E}_s$ from nearby particles, and a correction term $\boldsymbol{E}_c$ to eliminate overlap between the two components. The total electric field at the particle position is thus given by

$$\boldsymbol{E}_{@p} = \boldsymbol{E}_{l@p} + \boldsymbol{E}_s + \boldsymbol{E}_c. \tag{2.5}$$

The Eulerian electric field on the fluid grid, $\boldsymbol{E}_l$, is obtained by solving the Poisson equation for the electric potential:

$$\nabla^2\varphi = -\frac{\rho_e}{\varepsilon_0}, \quad \boldsymbol{E}_l = -\nabla\varphi, \tag{2.6}$$

where φ is the electric potential, and ρ_e is the charge density projected onto the fluid mesh based on particle positions and charges. Equation (2.6) is solved with periodic boundary conditions in the streamwise and spanwise directions, and zero-potential Dirichlet conditions at the top and bottom walls, which are assumed to be electrically grounded (i.e. $\varphi = 0$). Once the potential is obtained, the electric field $\boldsymbol{E}_l$ is evaluated and interpolated to particle locations to yield the long-range component $\boldsymbol{E}_{l@p}$.

For a particle i located within a grid cell A at position $\boldsymbol{x}_i$, the short-range field $\boldsymbol{E}_{s,i}$ is computed by summing the Coulombic contributions from all neighbouring particles j (with $j \neq i$) in cell A and its adjacent cells, using their positions $\boldsymbol{x}_j$ and charges q_j, as

$$\boldsymbol{E}_{s,i} = \frac{1}{4\pi\varepsilon_0}\sum_{j\neq i} q_j \frac{\boldsymbol{x}_i - \boldsymbol{x}_j}{|\boldsymbol{x}_i - \boldsymbol{x}_j|^3}. \tag{2.7}$$

Since the long-range and short-range components partially overlap, a correction term $\boldsymbol{E}_c$ is introduced. Assuming a grid cell A with neighbouring cells B_k, each containing a total charge q_k located at $\boldsymbol{x}_k$, and denoting the position of the centre of cell A as $\boldsymbol{x}_A$, the correction is given by

$$\boldsymbol{E}_c = -\frac{1}{4\pi\varepsilon_0}\sum_{k} q_k \frac{\boldsymbol{x}_A - \boldsymbol{x}_k}{|\boldsymbol{x}_A - \boldsymbol{x}_k|^3}. \tag{2.8}$$

After evaluating the particle trajectories, the feedback force per fluid density from the particles to the fluid phase, denoted by $\boldsymbol{f}$, can be computed. The drag force exerted on particle k is given by

$$\boldsymbol{F}_k = \zeta m_{p,k} \frac{\boldsymbol{u}_{f@p,k} - \boldsymbol{u}_{p,k}}{t_p}. \tag{2.9}$$

https://doi.org/10.1017/jfm.2025.10990 Published online by Cambridge University Press

According to Newton's third law, the reaction force acting on the fluid is $-\boldsymbol{F}_k$. To properly impose this reaction force onto the Eulerian grid in a physically consistent manner, we adopt a projection-based interpolation method (Richter & Sullivan 2013; Zheng, Feng & Wang 2021; Gao, Samtaney & Richter 2023). Specifically, the force $\boldsymbol{F}_k$ is distributed to the eight surrounding fluid grid nodes of particle k using a Gaussian-type weight function $\xi(k, j)$ based on the distance between particle k and grid node j. The resulting force per fluid density contribution from particle k to grid node j is then expressed as

$$\boldsymbol{f}_{j\leftarrow k} = -\frac{\xi(k, j)}{\rho_f V_k}\boldsymbol{F}_k, \tag{2.10}$$

where V_k is the volume formed by the eight grid nodes surrounding particle k.

The total feedback force at grid node j is obtained by summing over all nearby particles:

$$\boldsymbol{f}_j = \sum_{k=1}^{N(j)} \boldsymbol{f}_{j\leftarrow k} = -\sum_{k=1}^{N(j)} \frac{\xi(k, j)}{\rho_f V_k}\boldsymbol{F}_k, \tag{2.11}$$

where $N(j)$ denotes the number of particles contributing to node j.

For the particulate phase, periodic boundary conditions are imposed in the streamwise and spanwise directions. The top and bottom walls are treated as fully elastic, reflective boundaries. Collisions between particles are assumed to be perfectly elastic and are modelled using a 'hard-sphere' approach, in which particles are rigid, collisions are instantaneous, and total linear momentum is conserved before and after impact (Grosshans & Papalexandris 2017; Johnson, Bassenne & Moin 2020).

Given the dilute nature of the particulate phase, only binary collisions are considered. Let $\boldsymbol{u}_1$ and $\boldsymbol{u}_2$ denote the velocities, and $\boldsymbol{r}_1$ and $\boldsymbol{r}_2$ the positions, of particles 1 and 2 before the collision. The unit vector directed from the centre of particle 2 to that of particle 1 is defined as

$$\boldsymbol{n} = \frac{\boldsymbol{r}_1 - \boldsymbol{r}_2}{|\boldsymbol{r}_1 - \boldsymbol{r}_2|}. \tag{2.12}$$

The velocity of the ith particle, $\boldsymbol{u}_i$, can be projected onto a component parallel to $\boldsymbol{n}$:

$$\boldsymbol{u}_{i,n} = (\boldsymbol{u}_i \cdot \boldsymbol{n})\boldsymbol{n}. \tag{2.13}$$

After the collision, the velocities of particles 1 and 2, denoted by $\boldsymbol{u}_1^*$ and $\boldsymbol{u}_2^*$, are given by

$$\boldsymbol{u}_1^* = \boldsymbol{u}_1 - \frac{2}{1 + m_1/m_2}(\boldsymbol{u}_{1,n} - \boldsymbol{u}_{2,n}), \tag{2.14}$$

$$\boldsymbol{u}_2^* = \boldsymbol{u}_2 + \frac{2}{1 + m_2/m_1}(\boldsymbol{u}_{1,n} - \boldsymbol{u}_{2,n}), \tag{2.15}$$

where m_1 and m_2 are the masses of particles 1 and 2, respectively.

The particulate phase embedded in the turbulence is bidisperse, consisting of two species with equal number and mass density but differing in size. The particle-to-fluid density ratio is set to $\rho_p/\rho_f = 2200$, corresponding to the typical value for sand and air in natural dust storms (Zheng 2009). The normalised diameters and aerodynamic Stokes numbers of the smaller (larger) particles are $d_{p,<}^+ = 0.4$ ($d_{p,>}^+ = 0.7$) and $St_<^+ = 20$ ($St_>^+ = 60$), respectively. Here and throughout, subscripts $<$ and $>$ denote smaller and larger particles, respectively. The two species carry equal but opposite charges, with the

https://doi.org/10.1017/jfm.2025.10990 Published online by Cambridge University Press

St^+	d_p^+	ρ_p/ρ_f	Φ_V ($\times 10^{-4}$)	Φ_m	$\overline{St}_{el}^2$
20	0.4	2200	0.186 : 0.095 : 0.759	0.041 : 0.021 : 0.167	{0, 1.0 : 0.2 : 3.0, 4.0 : 1.0 : 8.0}
60	0.7	2200	0.977 : 0.486 : 3.895	0.215 : 0.107 : 0.857	{0, 1.732 : 0.346 : 5.192, 6.928 : 1.732 : 13.856}

Table 2. Key parameters of the particles used in the 119 simulation cases. Here, Φ_m, Φ_V and $\overline{St}_{el}^2$ represent the bulk mean particle mass loading, volume fraction and squared electrical Stokes number of each particle species, respectively. For example, $\Phi_m = 0.041 : 0.021 : 0.167$ indicates a parameter sweep from 0.041 to 0.167 with increment 0.021; similar notation applies to the other quantities.

smaller (larger) particles being negatively (positively) charged (e.g. Zheng *et al.* 2003; Forward, Lacks & Sankaran 2009). We perform simulations for a total of 119 cases, covering 7 different particle mass loadings, and 17 different electrical Stokes numbers (see table 2 for the details). The bulk mean total particle mass loading (hereafter referred to as particle mass loading) Φ_m increases from 0.256 to 1.024 in increments of approximately 0.128, while the bulk mean squared electrical Stokes number $\overline{St}_{el,<}^2$ ($\overline{St}_{el,>}^2$) varies from 0 (0) to 8.0 (13.856) in increments of 1.0 (1.732). Here, the overline $\overline{(\cdot)}$ denotes a bulk mean over the entire computational domain. To resolve the strongly nonlinear behaviour and precisely locate the phase boundary between turbulent and laminar regimes, additional simulations were performed with finer parameter increments, sweeping $\overline{St}_{el,<}^2$ ($\overline{St}_{el,>}^2$) from 1.0 (1.732) to 3.0 (5.192) in steps of 0.2 (0.346). Note that we hereafter use only $\overline{St}_{el,<}^2$ to characterise the strength of electrical effects, since the ratio $\overline{St}_{el,<}^2/\overline{St}_{el,>}^2$ is identically equal to 0.577.

The particle-laden turbulent flows are simulated up to a dimensionless time $t^+ \equiv t/t_\nu = 15\,000$ (equivalent to $t^* \equiv tU_b/\delta = 83.33$), using a fixed time step $\Delta t^+ = 0.01$ (i.e. $\Delta t^* = 0.00056$). This duration ensures that the simulations reach a statistically stationary state. Fluid and particle statistics are computed over $t^+ \in [10\,000, 15\,000]$ from 11 snapshots, averaged in time and over the wall-parallel (x–z) plane. It is important to note that for the purpose of facilitating comparison across different simulation cases, all statistical quantities presented in this study are normalised using the viscous scales of the particle-free reference flow. As confirmed in our previous study (Zhang *et al.* 2023), the computed first- and second-order statistics for both phases are in excellent agreement with benchmark results reported in earlier studies, validating the accuracy of the numerical model. To further examine the temporal evolution of the self-sustaining cycle under electrical effects, extended simulations were performed for four representative cases: $\Phi_m = 0.512$ and 0.768, each with $\overline{St}_{el,<}^2 = 2.0$ and 2.2. For these cases, the total simulation time was increased to $t^+ = 30\,000$ (i.e. $t^* = 166.67$).

3. Results

This section first presents the variations in fluid and particulate statistics with the electrical Stokes number $\overline{St}_{el,<}^2$ for two representative particle mass loadings, $\Phi_m = 0.512$ and 0.768. It should be noted that similar trends with increasing $\overline{St}_{el,<}^2$ are also observed for other particle mass loadings, but are not included here for clarity. A phase diagram based on 119 simulation cases is then shown in the parameter space defined by Φ_m and $\overline{St}_{el,<}^2$, along with a quantitative analysis of the underlying physical mechanisms.

https://doi.org/10.1017/jfm.2025.10990 Published online by Cambridge University Press

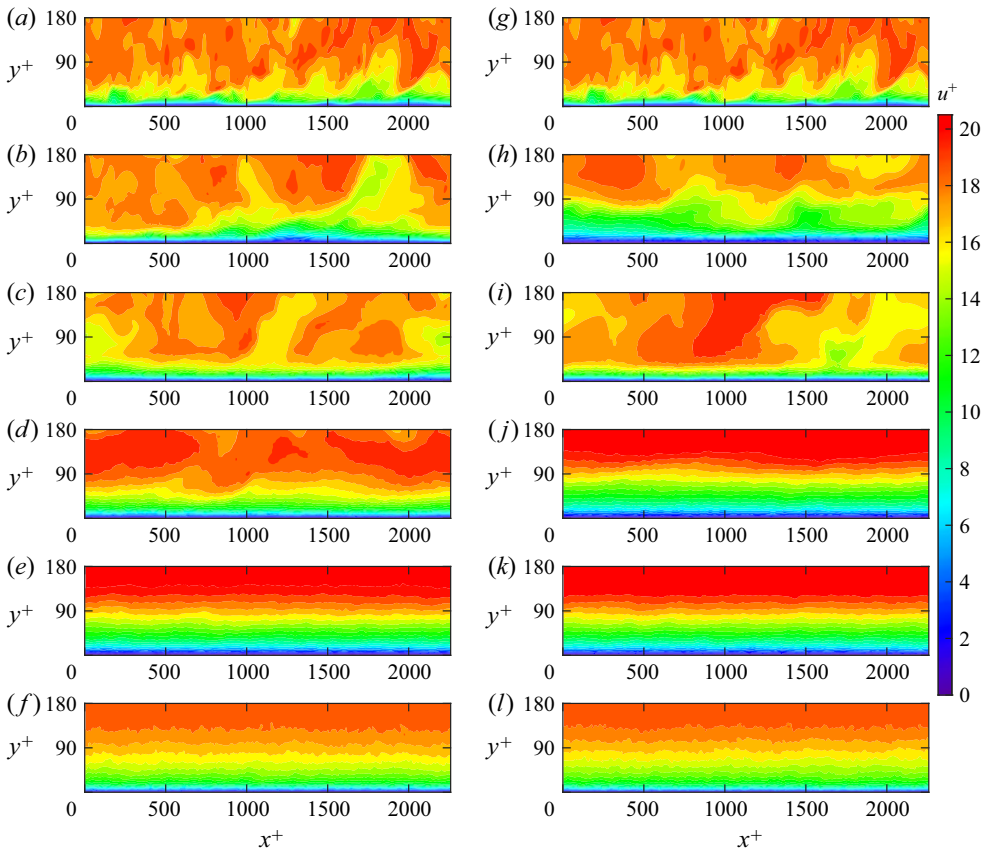


Figure 1. Snapshots of instantaneous streamwise fluid velocity in the streamwise–wall-normal plane at $z^+ = 0$ and $t^+ = 15\,000$, for fixed particle mass loadings (*a–f*) $\Phi_m = 0.512$ and (*g–l*) $\Phi_m = 0.768$. Here, (*a*,*g*) show the particle-free flow, while the particle-laden cases correspond to (*b*,*h*) $\overline{St}^2_{el,<} = 0$, (*c*,*i*) $\overline{St}^2_{el,<} = 1.0$, (*d*,*j*) $\overline{St}^2_{el,<} = 2.0$, (*e*,*k*) $\overline{St}^2_{el,<} = 2.2$, and (*f*,*l*) $\overline{St}^2_{el,<} = 8.0$.

3.1. *Fluid statistics of representative cases*

We begin by examining whether electrical effects significantly influence turbulent channel flow. Without loss of generality, figure 1 presents snapshots of instantaneous streamwise fluid velocity in the streamwise–wall-normal plane for several representative cases at particle mass loadings $\Phi_m = 0.512$ and 0.768. Compared to the particle-free flow (figure 1*a*,*g*), the presence of uncharged particles noticeably suppresses small-scale turbulent structures, reducing flow randomness and mixing (figure 1*b*,*h*). When particles are electrically charged, the flow becomes progressively more ordered with increasing electrical Stokes number $\overline{St}^2_{el,<}$ (figure 1*c–f*,*i–l*). In particular, when $\overline{St}^2_{el,<} = 2.2$, the flow undergoes relaminarisation, where the fluid travels smoothly, with no irregular fluctuations and mixing between adjacent layers (figure 1*e*,*k*). These observations demonstrate that under typical conditions, self-induced electrical effects can trigger a turbulence-to-laminar transition in particle-laden flows.

To quantitatively assess the role of electrical effects in fluid flow, the variation of mean streamwise fluid velocity and turbulent Reynolds stress with electrical Stokes number $\overline{St}^2_{el,<}$ is also presented in figures 2 and 3. As shown in figure 2, with increasing $\overline{St}^2_{el,<}$,

https://doi.org/10.1017/jfm.2025.10990 Published online by Cambridge University Press

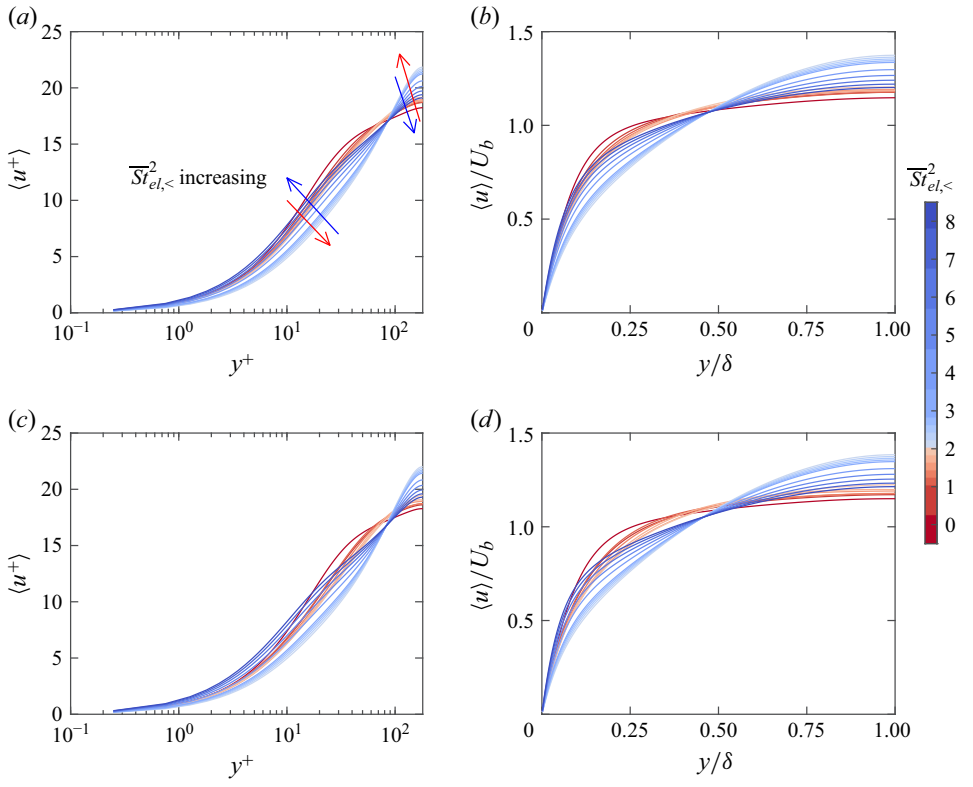


Figure 2. Wall-normal profiles of the (*a*) inner-scaled and (*b*) outer-scaled mean streamwise fluid velocity, $\langle u^+ \rangle$ and $\langle u \rangle / U_b$, for various cases at particle mass loading $\Phi_m = 0.512$, with electrical Stokes numbers $\overline{St}^2_{el,<}$ ranging from 0 to 8.0. (*c*,*d*) Same as (*a*,*b*), but for $\Phi_m = 0.768$.

the variation in mean streamwise fluid velocity exhibits a non-monotonic trend for both particle mass loadings. When $\overline{St}^2_{el,<} \leq 2.0$, corresponding to the turbulent regime, the mean streamwise fluid velocity profiles intersect at a common wall-normal location $y^+ \approx 72$ (or $y/\delta \approx 0.41$), referred to as the focus, where the mean streamwise fluid velocity becomes independent of $\overline{St}^2_{el,<}$. Above this focus, the mean streamwise velocity increases with increasing $\overline{St}^2_{el,<}$, whereas below it, the velocity decreases. When $\overline{St}^2_{el,<} > 2.0$, the flow undergoes relaminarisation, accompanied by abrupt changes in the mean streamwise fluid velocity profiles. Although the profiles again intersect at a secondary focus at $y^+ \approx 86$ (or $y/\delta \approx 0.48$), the variation trend is reversed relative to the turbulent cases: above the secondary focus, the mean streamwise fluid velocity decreases with increasing $\overline{St}^2_{el,<}$, while below it, the velocity increases. The emergence of a velocity focus in the mean streamwise velocity profile reflects the strong feedback exerted by particles on the carrier fluid flow due to electrical effects. This phenomenon is certainly linked to the influence of electrostatic forces on the wall-normal transport of particles. To interpret the presence of velocity focus, the wall-normal distributions of particle mass loading and feedback force as functions of the electrical Stokes number will be examined in detail in § 3.2.

Note that the wall-normal profiles of mean streamwise fluid velocity differ markedly between the turbulent and laminar regimes. This contrast arises from the enhanced momentum mixing associated with turbulence, which steepens the near-wall velocity gradient and flattens the velocity profile near the channel centre (Pope 2000).

https://doi.org/10.1017/jfm.2025.10990 Published online by Cambridge University Press

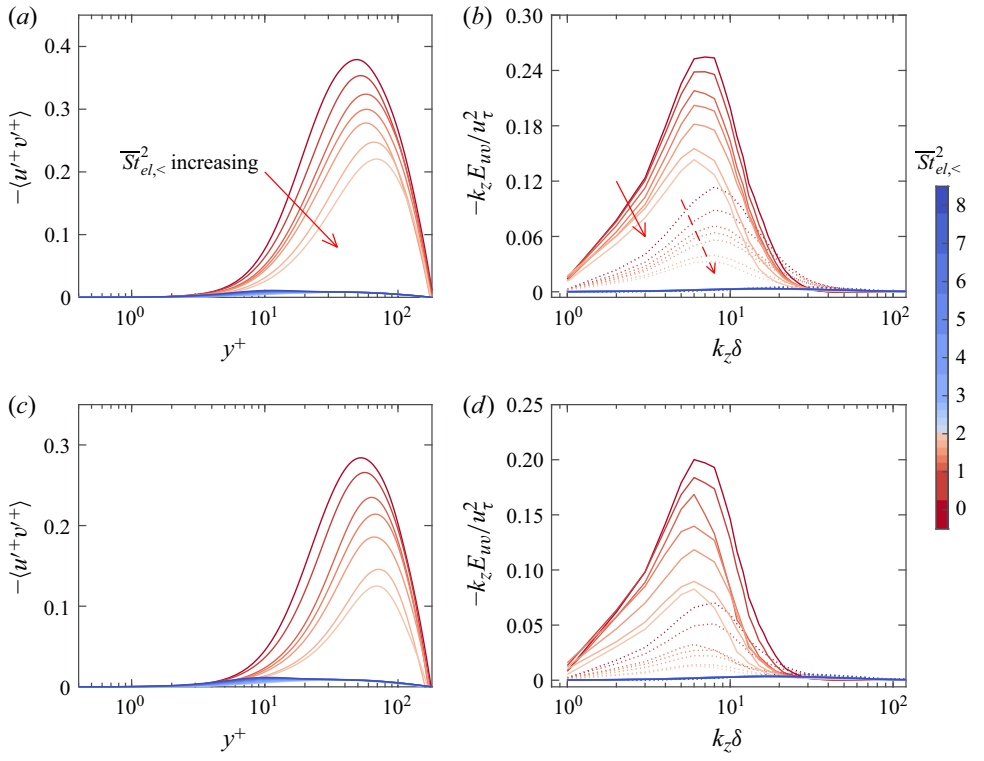


Figure 3. (*a*) Wall-normal profiles of the turbulent Reynolds stress $-\langle u'^+v'^+\rangle$ and (*b*) their premultiplied spanwise spectra $-k_zE_{uv}/u_\tau^2$ at $y^+ = 15$ (solid lines) and $y^+ = 54$ (dotted lines) for $\Phi_m = 0.512$, where k_z denotes the spanwise wavenumber. (*c*,*d*) Same as (*a*,*b*), but for $\Phi_m = 0.768$.

With increasing $\overline{St}^2_{el,<}$, the turbulent Reynolds stress progressively decreases in magnitude, and its peak shifts towards the channel centreline (see figure 3*a*,*c*). When $\overline{St}^2_{el,<}$ reaches 2.2, marking the onset of relaminarisation, the Reynolds stress abruptly vanishes throughout the channel, and all profiles collapse onto a single curve. Further insight into the scale-dependent influence of electrical effects is provided by the premultiplied spectra of Reynolds stress $-k_zE_{uv}/u_\tau^2$ (see figure 3*b*,*d*). These spectra show that electrical effects not only suppress the overall Reynolds stress intensity, but also shift its spectral peak towards larger scales (i.e. lower wavenumbers), indicating preferential suppression of small-scale fluctuations by small, charged inertial particles. This trend is consistent with the observations in figure 1.

Figure 4 displays the evolution of the inner-scaled streamwise velocity spectra, E_{uu}/u_τ^2, at $y^+ = 178$, as a function of the electrical Stokes number $\overline{St}^2_{el,<}$, for particle mass loadings $\Phi_m = 0.512$ and 0.768. In the turbulent regime, despite subtle variations with increasing $\overline{St}^2_{el,<}$, the spectra consistently decrease for $k_x\delta \lesssim 25$ but increase for $k_x\delta \gtrsim 25$. The phenomenon in which small-scale turbulent activity is enhanced while large-scale motions are suppressed due to the presence of 'point' and 'gravity-free' particles is referred to as the 'pivoting effect' (Poelma & Ooms 2006; Brandt & Coletti 2022). Boivin, Simonin & Squires (1998) demonstrated this effect by analysing the spectral distribution of energy exchange between the fluid and particles. In the low-wavenumber range, turbulent kinetic energy is transferred from the fluid to the particles, indicating that particles act as sinks of energy. In contrast, in the high-wavenumber range, the energy exchange rate becomes

https://doi.org/10.1017/jfm.2025.10990 Published online by Cambridge University Press

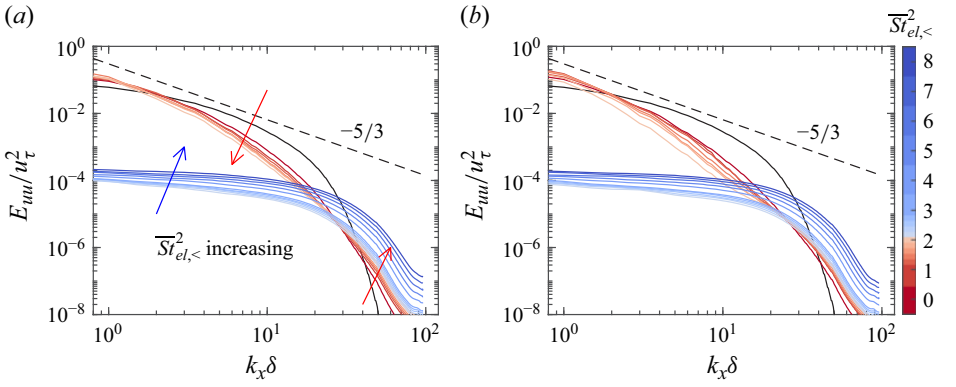


Figure 4. Inner-scaled streamwise velocity spectra E_{uu}/u_τ^2 at $y^+ = 178$ for particle mass loadings (*a*) $\Phi_m = 0.512$ and (*b*) $\Phi_m = 0.768$. Solid black lines denote the spectra of the particle-free flow, while dashed lines indicate the reference Kolmogorov $-5/3$ power law.

positive, suggesting that particles are capable of injecting energy into the turbulence. This particle-released energy is not immediately dissipated by viscous effects, thereby leading to an increase in small-scale turbulence intensity relative to the particle-free case. This mechanism can be interpreted through the following physical picture (Ferrante & Elghobashi 2003): small particles closely follow fluid parcel trajectories but generally possess higher kinetic energy than the surrounding fluid, allowing them to transfer energy to the flow. Upon entering a vortex, particles rapidly accelerate to match the local fluid velocity. After acceleration, despite their small but finite inertia, the particles retain their velocity longer than the surrounding fluid, resulting in a higher mean kinetic energy. Prior studies have shown that the pivoting effect becomes more pronounced with increasing particle mass loading (e.g. Squires & Eaton 1990; Boivin *et al.* 1998; Sundaram & Collins 1999). The present study further reveals that this effect is also enhanced with increasing electrical Stokes number, primarily due to the electrostatically induced redistribution of particle mass loading. A detailed analysis is presented in § 3.2.

As expected, a sharp spectral transition occurs in figure 4 when $\overline{St}^2_{el,<}$ reaches 2.2, indicating the onset of relaminarisation. In the large-scale range (i.e. $k_x\delta \lesssim 10$), the spectral energy drops to the order of 10^{-4} and remains nearly constant, with a reduction of more than three orders of magnitude at $k_x\delta \approx 1$. In contrast, at smaller scales (i.e. $k_x\delta \gtrsim 30$), the spectral energy in the laminar regime exceeds that in the turbulent regime. Notably, this spectral trend becomes increasingly pronounced with higher $\overline{St}^2_{el,<}$, suggesting that electrical effects tend to promote a more uniform distribution of turbulent kinetic energy across scales.

3.2. *Particle statistics of representative cases*

To further explain how electrical effects modulate turbulence, relevant particle statistics are presented. Figures 5 and 6 show the wall-normal profiles of various particle velocity statistics at $\Phi_m = 0.512$ and 0.768, respectively, across cases with varying electrical Stokes numbers. It is evident that electrical effects significantly modify both the mean and fluctuating components of particle velocity. For the mean streamwise particle velocity $\langle u_p^+ \rangle$, root mean square (r.m.s.) streamwise particle fluctuating velocity $u'^+_{p,rms}$, and particle Reynolds stress $-\langle u_p'^+ v_p'^+ \rangle$, sharp transitions are observed as the flow transitions from turbulent to laminar (figures 5(*a*,*b*,*d*) and 6(*a*,*b*,*d*)). In particular, within laminar

https://doi.org/10.1017/jfm.2025.10990 Published online by Cambridge University Press

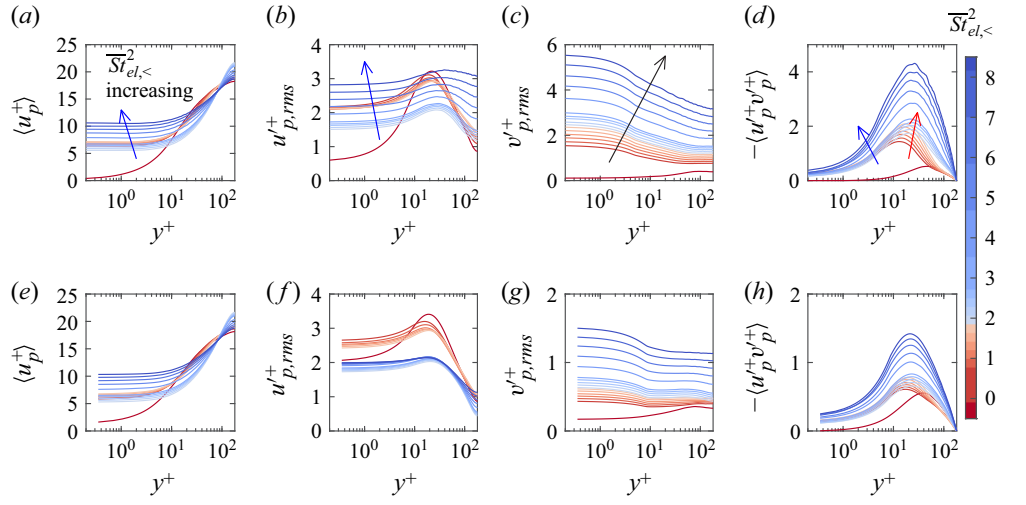


Figure 5. Wall-normal profiles of particle velocity statistics at $\Phi_m = 0.512$ for varying squared electrical Stokes numbers: (*a*) mean streamwise particle velocity $\langle u_p^+ \rangle$; (*b*) r.m.s. streamwise particle velocity fluctuation $u'^+_{p,rms}$; (*c*) r.m.s. wall-normal particle velocity fluctuation $v'^+_{p,rms}$; and (*d*) particle Reynolds stress $-\langle u_p'^+ v_p'^+ \rangle$ for the smaller particles. (*e–h*) Same quantities as in (*a–d*), respectively, but for the larger particles.

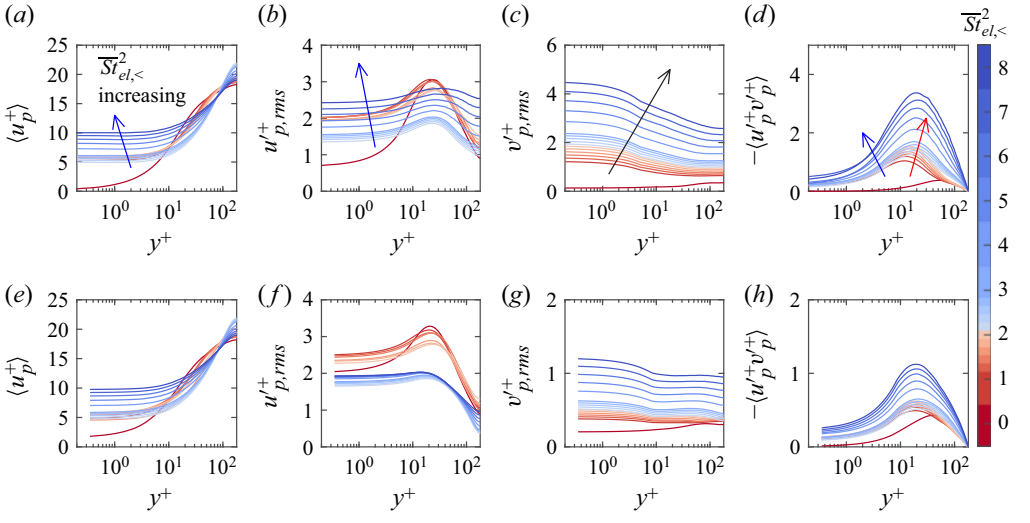


Figure 6. Wall-normal profiles of particle velocity statistics at $\Phi_m = 0.768$ for varying squared electrical Stokes numbers. (*a*) Mean streamwise particle velocity $\langle u_p^+ \rangle$; (*b*) r.m.s. streamwise particle velocity fluctuation $u'^+_{p,rms}$; (*c*) r.m.s. wall-normal particle velocity fluctuation $v'^+_{p,rms}$; and (*d*) particle Reynolds stress $-\langle u_p'^+ v_p'^+ \rangle$ for the smaller particles. (*e–h*) Same quantities as in (*a–d*), respectively, but for the larger particles.

regimes, particle velocity fluctuations tend to increase with increasing electrical Stokes number, although this trend does not hold consistently in turbulent regimes. By contrast, the r.m.s. wall-normal particle fluctuating velocity $v'^+_{p,rms}$ increases monotonically with electrical Stokes number $\overline{St}^2_{el,<}$ over the range $[0, 8]$ (figures 5(*c*) and 6(*c*)). This monotonic trend indicates that wall-normal particle dynamics are dominated by inter-particle electrostatic interactions in all simulated cases laden with charged particles, irrespective of the flow regime.

https://doi.org/10.1017/jfm.2025.10990 Published online by Cambridge University Press

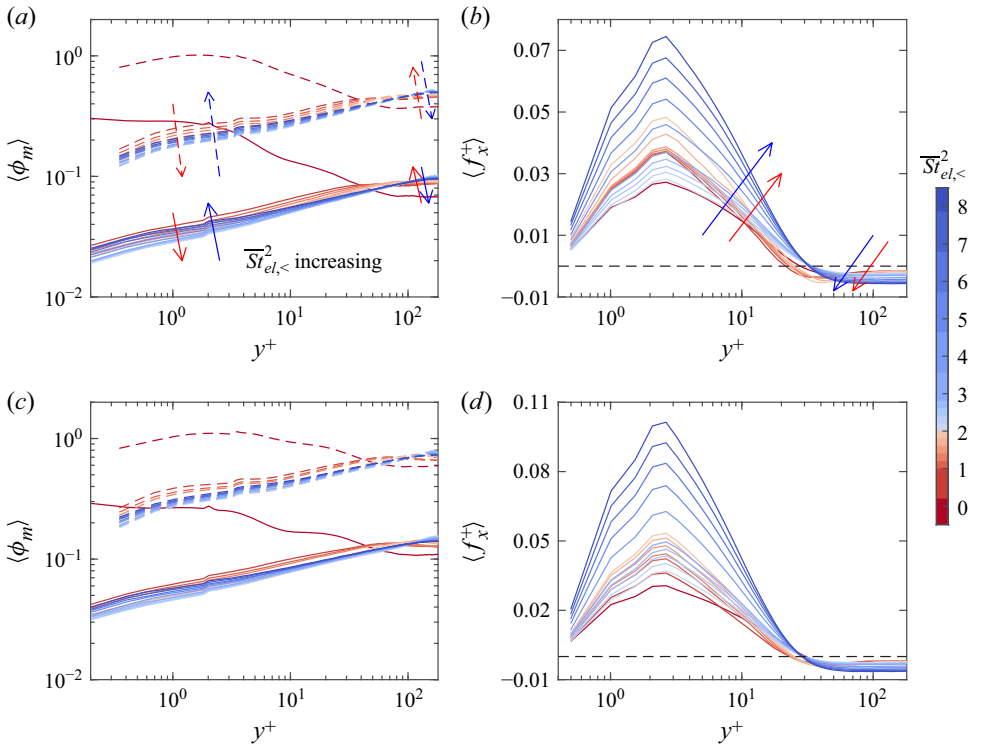


Figure 7. Wall-normal profiles of (*a*) the mean local particle mass loading $\langle\phi_m\rangle$ for small (solid lines) and large (dashed lines) particles, and (*b*) the mean normalised particle-to-fluid feedback force $\langle f_x^+\rangle \equiv \nu\langle f_x\rangle/u_\tau^3$ at $\Phi_m = 0.512$, for varying squared electrical Stokes numbers $\overline{St}^2_{el,<}$. (*c,d*) Same as (*a,b*), but for $\Phi_m = 0.768$.

Figure 7 shows the wall-normal profiles of the mean particle mass loading, $\langle\phi_m\rangle$, and the mean normalised streamwise feedback force, $\langle f_x^+\rangle$, for cases with $\Phi_m = 0.512$ and 0.768. In the turbulent regimes, as electrical effects intensify, $\langle\phi_m\rangle$ for both small and large particles decreases in the near-wall region, and increases in the outer region (figure 7*a,c*), indicating a redistribution of particles towards the channel centre, and suppression of near-wall accumulation. In contrast, the laminar regime exhibits the opposite trend. Particle mass loading $\langle\phi_m\rangle$ for both small and large particles increases with increasing $\overline{St}^2_{el,<}$ in the near-wall region, and decreases in the outer region, reflecting particle migration towards the wall, and enhanced near-wall accumulation.

To explain the opposite trends in particle mass loading observed between turbulent and laminar regimes, we examine three phoresis integrals that determine the wall-normal distribution of particle concentration (Zhang *et al.* 2023):

$$n(y,t) \propto \exp\left(I_{bias} + I_{elec} + I_{turbo}\right), \tag{3.1}$$

where I_{bias}, I_{elec} and I_{turbo} represent the contributions from biased sampling of the fluid velocity by particles, electrostatic drift of charged particles, and turbophoresis, respectively. These integrals are defined as

$$I_{bias} = \frac{1}{t_p}\int_0^y \frac{\langle \zeta\, v_{f@p}|\xi\rangle}{\langle v_p^2|\xi\rangle}\,\mathrm{d}\xi, \tag{3.2}$$

$$I_{elec} = \frac{q}{m_p}\int_0^y \frac{\langle E_{y@p}|\xi\rangle}{\langle v_p^2|\xi\rangle}\,\mathrm{d}\xi, \tag{3.3}$$

https://doi.org/10.1017/jfm.2025.10990 Published online by Cambridge University Press

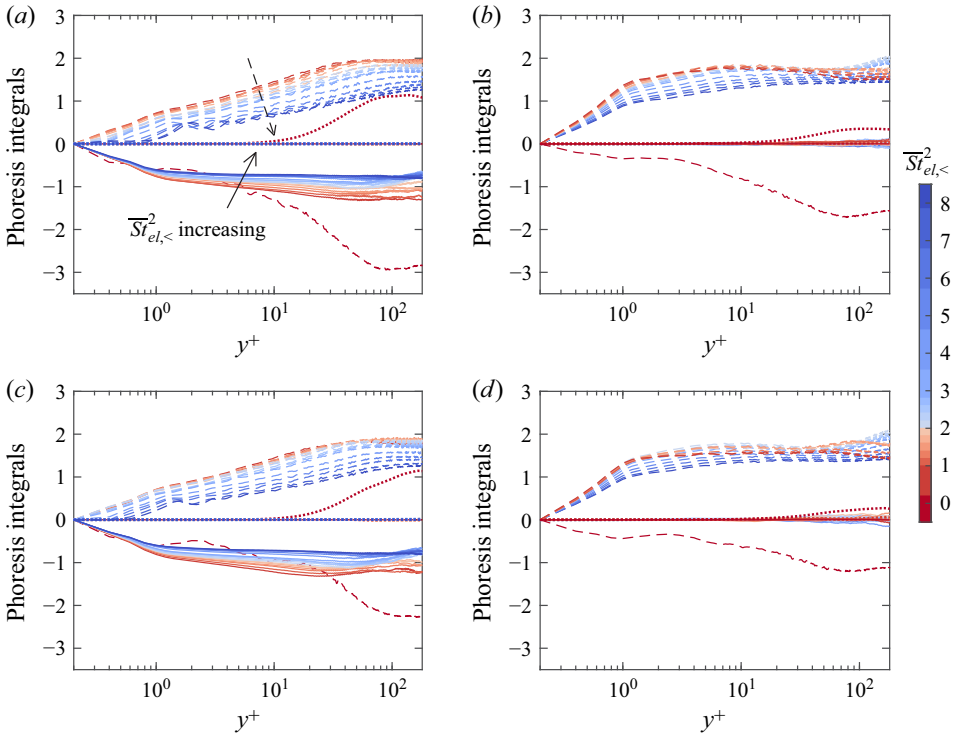


Figure 8. Wall-normal profiles of the phoretic integrals for (*a*) small and (*b*) large particles at $\Phi_m = 0.512$, and (*c*) small and (*d*) large particles at $\Phi_m = 0.768$. Dotted, solid and dashed lines represent I_{bias}, I_{elec} and I_{turbo}, respectively. Line colours correspond to different squared electrical Stokes numbers $\overline{St}^2_{el,<}$, as indicated in the colour bar.

$$I_{turbo} = -\int_0^y \frac{\mathrm{d}\ln\langle v_p^2|\xi\rangle}{\mathrm{d}\xi}\,\mathrm{d}\xi, \tag{3.4}$$

where $\langle\cdot|\xi\rangle$ denotes a conditional average taken over all particles located within a horizontal slab centred at $y = \xi$.

According to (3.1), the particle concentration profile is governed by the interplay among turbophoresis, biased sampling and electrostatic drift. Figure 8 shows the wall-normal distributions of the phoretic integrals for various $\overline{St}^2_{el,<}$ at $\Phi_m = 0.512$ and 0.768. In the absence of electrical effects, I_{bias} is positive beyond the viscous sublayer ($y^+ \gtrsim 5$), and increases monotonically with distance from the wall (see the darkest dashed lines in figure 8*a–d*), indicating that biased sampling drives particles away from the wall (Johnson *et al.* 2020). In contrast, when particles are electrically charged, I_{bias} remains identically zero throughout the channel, implying that particle mass loading (or concentration) is governed solely by the combined effects of turbophoresis and electrostatic drift. The suppression of I_{bias} arises because electrical effects promote a more homogeneous distribution of charged inertial particles (e.g. Alipchenkov *et al.* 2004; Lu *et al.* 2010; Zhang *et al.* 2023).

For smaller particles, when electrically charged, I_{turbo} is positive and increases with wall-normal distance (figure 8*a*,*c*), indicating that turbophoresis drives particles away from the wall, contrary to the uncharged case (darkest dashed line in figure 8*a*) or the case with very small electrical Stokes numbers reported by Zhang *et al.* (2023). This reversal of turbophoresis stems from the significant modification of wall-normal

https://doi.org/10.1017/jfm.2025.10990 Published online by Cambridge University Press

particle velocity fluctuations under electrical effects, whereby $v'^{+}_{p,rms}$ transitions from increasing to decreasing with y^+ (see figures 5(*c*,*g*) and 6(*c*,*g*)). Moreover, the electrostatic integral I_{elec} is negative and decreases with y^+, suggesting that the electric field induces particle migration towards the wall. In the turbulent regime (red lines), the turbophoretic contribution remains nearly invariant with increasing $\overline{St}^2_{el,<}$, while the wall-ward drift due to electrostatic forces is notably suppressed. Accordingly, near-wall particle concentration decreases and outer-layer concentration increases with increasing $\overline{St}^2_{el,<}$. In contrast, in the laminar regime (blue lines), increasing $\overline{St}^2_{el,<}$ leads to a substantial weakening of turbophoretic migration away from the wall, whereas the electrostatic drift towards the wall is only mildly reduced. In other words, although the wall-directed migration induced by the electric field becomes less effective as $\overline{St}^2_{el,<}$ increases, the suppression of the turbophoresis-driven outward migration is even more pronounced. As a result, compared to cases with weaker electrical effects, stronger $\overline{St}^2_{el,<}$ effectively introduces an additional net migration of particles towards the wall. Consequently, with increasing $\overline{St}^2_{el,<}$, smaller particles exhibit enhanced near-wall accumulation and diminished mass loading in the outer layer, opposite to the trend observed in the turbulent regime (figure 7*a*,*c*).

For larger particles, the concentration is governed solely by turbophoretic effects (figure 8*b*,*d*). In the turbulent regime (red lines), increasing $\overline{St}^2_{el,<}$ enhances turbophoresis-induced migration away from the wall in the outer region. As a result, large-particle mass loading decreases near the wall and increases further from the wall with increasing $\overline{St}^2_{el,<}$. In contrast, in the laminar regime (blue lines), turbophoretic migration in the outer region is significantly suppressed as $\overline{St}^2_{el,<}$ increases, leading to increased near-wall concentration and reduced outer-layer loading. The qualitative trend of mass loading variation with $\overline{St}^2_{el,<}$ for larger particles is consistent with that observed for smaller particles.

In short, the variation of particle mass loading with increasing $\overline{St}^2_{el,<}$, as shown in figure 8(*a*,*c*), can be attributed to distinct mechanisms in turbulent and laminar regimes. In the turbulent regime, the wall-ward migration of smaller particles due to electrostatic drift is significantly suppressed, whereas the turbophoretic migration of larger particles away from the wall is markedly enhanced in the outer region. These combined effects result in a net decrease in near-wall mass loading, and a corresponding increase in the outer layer. By contrast, in the laminar regime, turbophoretic migration away from the wall is substantially weakened for both smaller and larger particles, thereby leading to enhanced accumulation near the wall, and reduced concentration farther from it.

As shown in figure 7(*b*,*d*), the variations in particle velocity statistics (figures 5 and 6) and mass loadings (figure 7*a*,*c*) significantly modify the particle-to-fluid feedback force. In the near-wall region $y^+ \lesssim 20$ where $\langle f_x^+ \rangle$ is positive, the mean streamwise particle velocity exceeds that of the surrounding fluid, indicating that particles locally accelerate the flow (Gao *et al.* 2023; Cui *et al.* 2024). In contrast, in the outer region ($y^+ \gtrsim 30$), where $\langle f_x^+ \rangle$ becomes negative, particles move more slowly than the fluid, thereby exerting a decelerating effect. In the turbulent regime, the magnitude of $\langle f_x^+ \rangle$ increases monotonically with increasing $\overline{St}^2_{el,<}$. During the transition from turbulence to laminar flow, the magnitude of $\langle f_x^+ \rangle$ exhibits a sharp drop, followed by continued monotonic growth with increasing $\overline{St}^2_{el,<}$ in the laminar regime. It is evident that the increasing magnitude of $\langle f_x^+ \rangle$ with $\overline{St}^2_{el,<}$, together with its opposite signs in the inner and outer regions, causes the $\langle f_x^+ \rangle$ profiles to intersect at a common wall-normal location where $\langle f_x^+ \rangle$ approaches zero, irrespective of whether the flow is laminar or turbulent.

https://doi.org/10.1017/jfm.2025.10990 Published online by Cambridge University Press

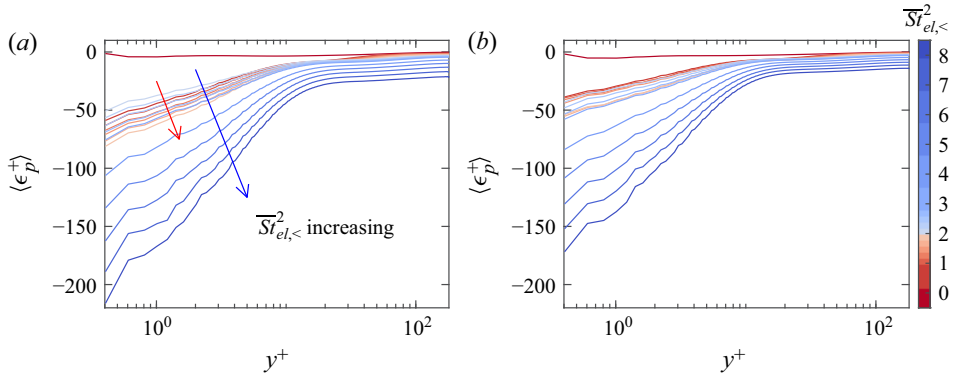


Figure 9. Wall-normal profiles of the normalised particle-induced extra dissipation of the kinetic energy $\langle \epsilon_p^+ \rangle$ at (*a*) $\Phi_m = 0.512$ and (*b*) $\Phi_m = 0.768$ for varying squared electrical Stokes numbers $\overline{St}^2_{el,<}$.

This intersection is the underlying reason for the emergence of the velocity focus observed in figure 2.

The presence of particles can induce extra dissipation of turbulent kinetic energy, which is formulated by considering both the work done by the particles on the local fluid and the work by the local fluid on the particles (e.g. Zhao, Andersson & Gillissen 2013). By definition, the rate of work exerted by the local fluid on a particle is given by $m_p \zeta / t_p (\boldsymbol{u}_{f@p} - \boldsymbol{u}_p) \cdot \boldsymbol{u}_p$, where m_p is the particle mass. According to Newton's third law, the rate of work done by the particle on the local fluid takes the form $-m_p \zeta / t_p (\boldsymbol{u}_{f@p} - \boldsymbol{u}_p) \cdot \boldsymbol{u}_{f@p}$. The extra dissipation of turbulent kinetic energy is the sum of the above two contributions, and therefore can be expressed in dimensionless form normalised by viscous scales as

$$\langle \epsilon_p{}^+ \rangle = \langle \zeta \left(\boldsymbol{u}^+_{f@p} - \boldsymbol{u}^+_p \right) \cdot \left(\boldsymbol{u}^+_p - \boldsymbol{u}^+_{f@p} \right) \rangle. \tag{3.5}$$

In addition, the electrical effects are found to further enhance $\langle \epsilon_p^+ \rangle$, thus contributing to turbulence suppression (Cui *et al.* 2024). Figure 9 shows wall-normal profiles of particle-induced extra dissipation $\langle \epsilon_p^+ \rangle$ for mass loadings $\Phi_m = 0.512$ and 0.768 at various $\overline{St}^2_{el,<}$. Evidently, $\langle \epsilon_p^+ \rangle$ generally increases with increasing $\overline{St}^2_{el,<}$, except for an abrupt reduction at the turbulent-to-laminar transition. This behaviour explains the notable decrease in Reynolds stress with increasing $\overline{St}^2_{el,<}$ in the turbulent regimes illustrated in figure 3(*a*,*c*).

As shown in (3.5), the particle-induced extra dissipation, which is responsible for turbulence attenuation (Xia *et al.* 2022; Motoori & Goto 2025), depends on the relative (or slip) streamwise velocity between the carrier fluid and the particulate phase $\Delta u^+ = \langle u^+_{f@p} \rangle - \langle u^+_p \rangle$ (Yu *et al.* 2017). It is therefore essential to examine how electrical effects modify this relative velocity, and to uncover the underlying physical mechanism. Figure 10 presents wall-normal profiles of the mean relative streamwise velocity at two particle mass loadings and various values of $\overline{St}^2_{el,<}$. In the absence of electrical effects, the relative velocity is negative in the near-wall region, and positive in the bulk of the channel. This trend becomes more pronounced with increasing particle inertia. The observation that the mean particle velocity exceeds that of the surrounding fluid near the wall can be attributed to the fact that high-inertia particles retain a portion of their streamwise momentum as they approach the wall, and are not constrained by the no-slip condition (Vreman 2015; Yu *et al.* 2021).

https://doi.org/10.1017/jfm.2025.10990 Published online by Cambridge University Press

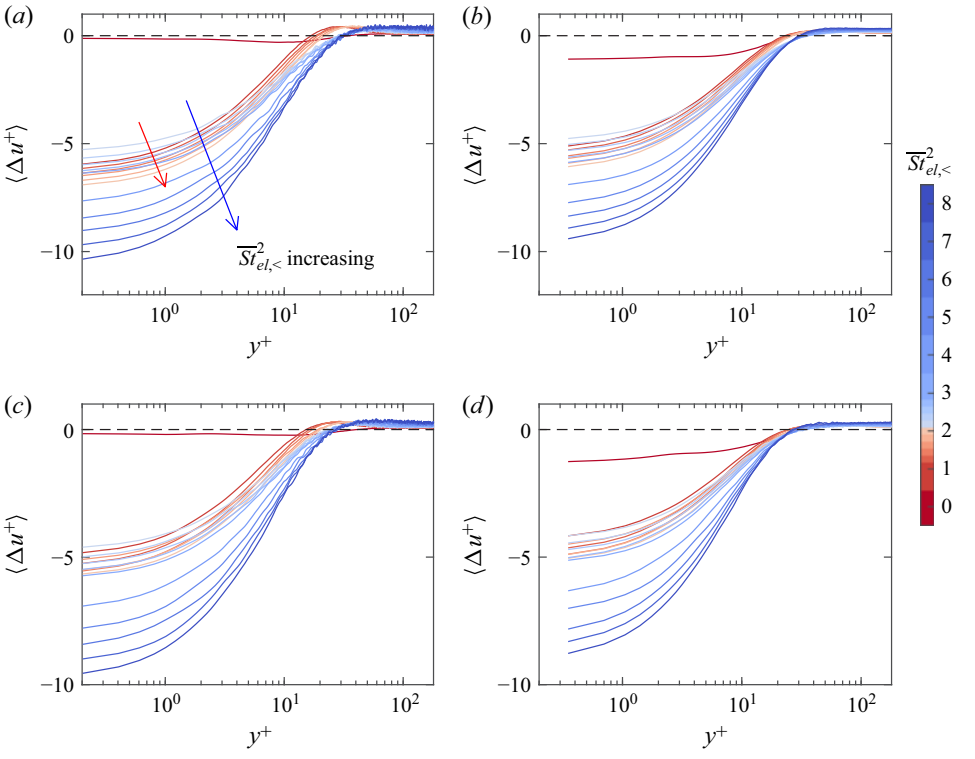


Figure 10. Wall-normal profiles of the mean relative streamwise velocity $\Delta u^+ = \langle u^+_{f@p} \rangle - \langle u^+_p \rangle$ for varying squared electrical Stokes numbers $\overline{St}^2_{el,<}$ at two particle mass loadings: $\Phi_m = 0.512$ for (*a*) small and (*b*) large particles, respectively; (*c*,*d*) same as (*a*,*b*) but at $\Phi_m = 0.768$.

As expected, the mean relative streamwise velocity Δu^+ increases with increasing $\overline{St}^2_{el,<}$, with the exception of an abrupt drop at the turbulence–laminar transition, reflecting the trend observed in the particle-induced extra dissipation. To elucidate the physical mechanism underlying this behaviour, we further analyse the fluid–particle velocity correlation (Boutsikakis *et al.* 2022)

$$R_{u'_p u'_{f@p}} = \frac{\langle u'_p u'_{f@p} \rangle}{\langle u'^2_p \rangle^{1/2} \langle u'^2_{f@p} \rangle^{1/2}}, \tag{3.6}$$

which quantifies the degree to which particles follow the fluid motion. As illustrated in figure 11, $R_{u'_p u'_{f@p}}$ decreases continuously with increasing $\overline{St}^2_{el,<}$ from 1 to 8, spanning both turbulent and laminar regimes. This monotonic decline indicates that electrical effects progressively weaken the coupling between particle and fluid velocity fields. In other words, particle dynamics become increasingly dominated by electrostatic forces, while their responsiveness to the fluid motion weakens. Consequently, the primary mechanism responsible for the increase in Δu^+ is the disruption of fluid–particle velocity correlation, which leads to kinematic decoupling between the two phases and thereby enhances the mean relative streamwise velocity.

https://doi.org/10.1017/jfm.2025.10990 Published online by Cambridge University Press

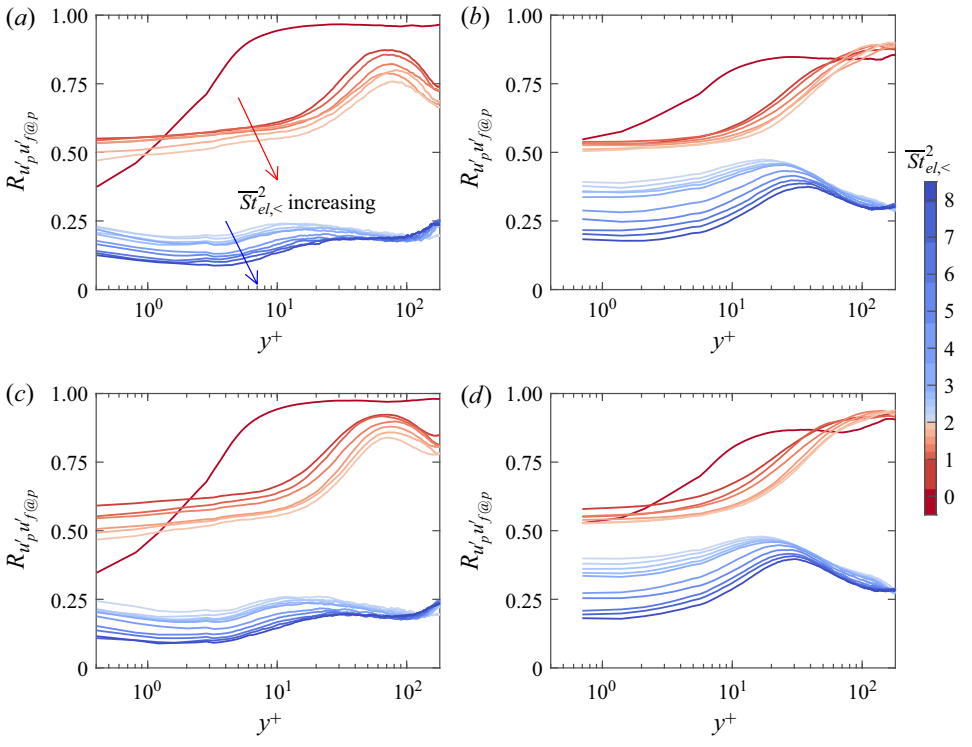


Figure 11. Wall-normal profiles of the fluid–particle velocity correlation $R_{u'_p u'_{f@p}}$ for varying squared electrical Stokes numbers $\overline{St}^2_{el,<}$ at two particle mass loadings: $\Phi_m = 0.512$ for (*a*) small and (*b*) large particles, respectively; (*c*,*d*) same as (*a*,*b*) but at $\Phi_m = 0.768$.

3.3. *Phase diagram and physical mechanisms*

Next, the phase diagram for all 119 simulated cases is depicted in figure 12. In addition to distinguishing turbulent and laminar regimes, the wall shear stress is quantitatively evaluated. The wall friction coefficient is defined as $C_f = 2\tau_w/(\rho_f U_b^2)$, where the wall shear stress τ_w is computed using a formulation analogous to the Fukagata–Iwamoto–Kasagi identity (Fukagata, Iwamoto & Kasagi 2002):

$$\tau_w = \frac{3}{\delta}\int_0^\delta \left(1 - \frac{y}{\delta}\right)\left(\tau_\nu + \tau_R + \tau_p\right) \mathrm{d}y, \tag{3.7}$$

with $\tau_\nu = \rho_f \nu(\partial\langle u\rangle/\partial y)$, $\tau_R = -\rho_f\langle u'v'\rangle$ and $\tau_p = \rho_f \int_\delta^y \langle f_x\rangle \,\mathrm{d}y$ representing the viscous, Reynolds and particle stresses, respectively. This formulation allows a quantitative decomposition of wall friction into its physical contributions.

As illustrated in figure 12, three distinct flow regimes emerge in the $(\Phi_m, \overline{St}^2_{el,<})$ parameter space: (I) a drag-reduced turbulent regime, where wall friction is lower than in the particle-free case and varies non-monotonically with both Φ_m and $\overline{St}^2_{el,<}$; (II) a drag-reduced laminar regime, exhibiting substantial drag reduction; and (III) a drag-enhanced laminar regime, associated with a pronounced drag increase. In contrast to regime I, wall drag in regimes II and III increases monotonically with both Φ_m and $\overline{St}^2_{el,<}$.

Having verified the importance of electrical effects, we now turn our attention to the physical mechanisms underlying relaminarisation. Specifically, we examine how electrical effects alter the near-wall self-sustaining cycle that maintains turbulence. As shown in

https://doi.org/10.1017/jfm.2025.10990 Published online by Cambridge University Press

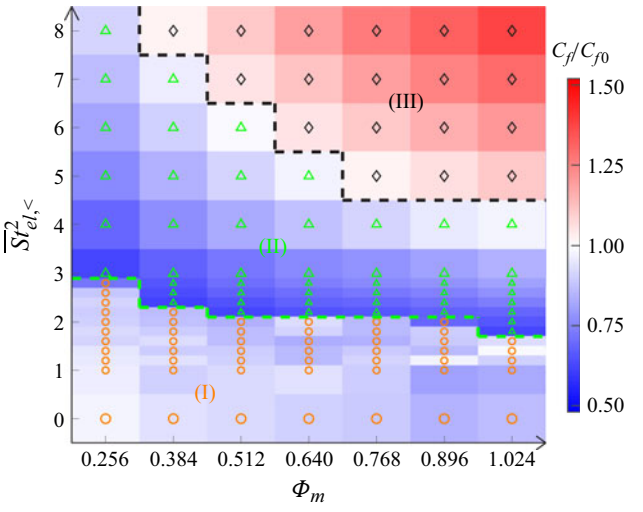


Figure 12. Phase diagram of particle-laden channel flow as a function of Φ_m and $\overline{St}^2_{el,<}$. Orange circles denote the drag-reduced turbulent regime, green triangles indicate the drag-reduced laminar regime, and black diamonds represent the drag-enhanced laminar regime. Background colour represents the ratio of the wall friction coefficient to that of the particle-free case, C_f/C_{f0}. The green (black) dashed line marks the phase boundary between flow regimes I and II (II and III).

figure 13(a), this cycle involves three successive processes: (1) the generation of streaks by streamwise vortices; (2) the breakdown of these streaks resulting from instability; and (3) the regeneration of streamwise vortices via nonlinear mechanisms (Hamilton, Kim & Waleffe 1995; Waleffe 1997; Reddy *et al.* 1998; Hwang & Cossu 2010). Numerical experiments reveal that interrupting any of these processes leads to relaminarisation (Jiménez & Pinelli 1999), indicating that turbulence is maintained only when these events occur in the correct sequence and on appropriate time scales (Hamilton *et al.* 1995).

Given the flow homogeneity in both the streamwise and spanwise directions, Fourier decomposition serves as an effective tool to investigate the self-sustaining cycle. Thus the modal r.m.s. velocity is defined as (Hamilton *et al.* 1995; Wang & Richter 2019; Lozano-Durán, Bae & Encinar 2020)

$$M(m\alpha, n\beta) = \left(\int_0^{L_y} |\widehat{\boldsymbol{u}'}(m\alpha, y, n\beta)|^2 \, \mathrm{d}y \right)^{1/2}, \tag{3.8}$$

where $\widehat{(\cdot)}$ denotes the Fourier mode, and $m, n \in \mathbb{Z}$ are modal indices corresponding to the fundamental wavenumbers $\alpha = 2\pi/L_x$ and $\beta = 2\pi/L_z$. Each mode $M(m\alpha, n\beta)$ corresponds to a specific flow structure. In particular, the mode $M(0, \beta)$ represents large-scale streaks that are uniform in the streamwise direction, while $M(\alpha, 0)$ corresponds to streaks that are elongated along the spanwise direction. This distinction arises because the zeroth and first Fourier modes represent spatial uniformity and the dominant periodic component, respectively. When the energy of the streamwise-uniform large-scale streaks $M(0, \beta)$ is transferred to other modes such as $M(\alpha, 0)$ and $M(\alpha, \beta)$, the streaks become unstable. Consequently, the superposition of these modes gives rise to meandering streak structures. A dimensionless modal r.m.s. velocity $M^*(m\alpha, n\beta)$ can be defined by normalising $M(m\alpha, n\beta)$ with $(U_b^2\delta)^{1/2}$.

As streamwise vortices convect downstream, they lift low-speed fluid away from the wall and push high-speed fluid towards it, thereby producing elongated streaks via the linear

https://doi.org/10.1017/jfm.2025.10990 Published online by Cambridge University Press

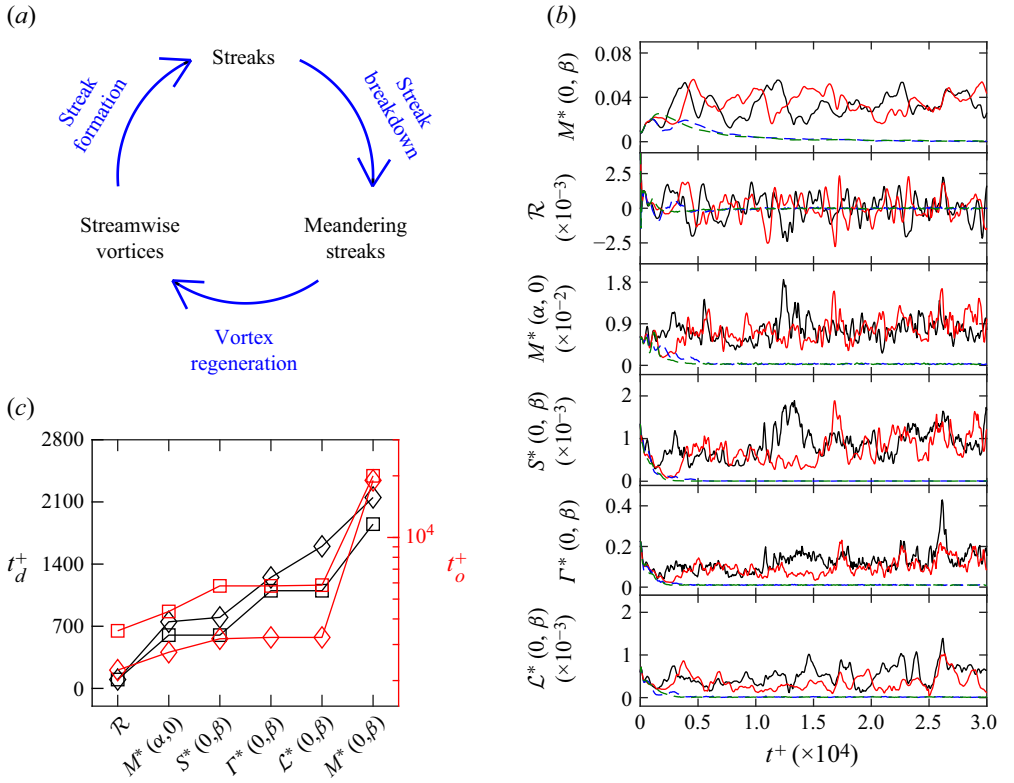


Figure 13. Influence of electrical effects on the near-wall self-sustaining cycle. (*a*) Schematic of the near-wall self-sustaining cycle. (*b*) Temporal evolution of key subprocesses for cases with $\overline{St}^2_{el,<} = 2.0$ (black solid lines) and $\overline{St}^2_{el,<} = 2.2$ (blue dashed lines) at $\Phi_m = 0.512$, and with $\overline{St}^2_{el,<} = 2.0$ (red solid lines) and $\overline{St}^2_{el,<} = 2.2$ (green dashed lines) at $\Phi_m = 0.768$. (*c*) For $\Phi_m = 0.512$, the initial time t_d^+ at which the evolution for $\overline{St}^2_{el,<} = 2.2$ deviates from that for $\overline{St}^2_{el,<} = 2.0$ is marked by black squares, and the onset time of full relaminarisation t_o^+ is indicated by red squares. For $\Phi_m = 0.768$, t_d^+ and t_o^+ are marked by black and red diamonds, respectively.

lift-up effect under mean shear. Streak formation via the lift-up effect requires that the streamwise vortices exceed a critical circulation threshold (Hamilton & Abernathy 1994; Hamilton *et al.* 1995). Thus the circulation of the streamwise vorticity mode $\widehat{\omega}_x(0, y, \beta)$ provides a suitable measure of vortex strength within the self-sustaining cycle:

$$\Gamma(0, \beta) = L_z \int_0^{L_y} \widehat{\omega}_x(0, y, \beta)\, \mathrm{d}y. \tag{3.9}$$

Its modulus quantifies the total strength of vortex-induced momentum transport, and a dimensionless form is given by $\Gamma^*(0, \beta) = |\Gamma(0, \beta)|/(U_b\delta)$.

The lift-up process can be expressed as a linear interaction between wall-normal velocity fluctuations and the mean shear. In physical space, the lift-up mechanism is represented by the term $-v'\,\partial\langle u\rangle/\partial y$ (Bakewell & Lumley 1967; Ellingsen & Palm 1975). Its Fourier counterpart, integrated in the wall-normal direction, yields

$$\mathcal{L}(0, \beta) = \int_0^{L_y} \widehat{v'}(0, y, \beta)\frac{\partial\langle u\rangle}{\partial y}\, \mathrm{d}y. \tag{3.10}$$

https://doi.org/10.1017/jfm.2025.10990 Published online by Cambridge University Press

The modulus $|\mathcal{L}(0,\beta)|$ characterises the efficiency of energy transfer from the mean shear to the streaks. Its dimensionless form reads $\mathcal{L}^*(0,\beta)=|\mathcal{L}(0,\beta)|/U_b^2$.

Once amplified by the lift-up effect, streaks undergo rapid meandering or oscillation motion, and eventually break down into smaller-scale turbulent structures due to streak instability (Hamilton *et al.* 1995; Waleffe 1997). When streaks break down, energy is redistributed from the dominant streak mode to newly generated three-dimensional perturbations. These perturbations subsequently grow and interact nonlinearly to regenerate streamwise vortices, thus completing the cycle. Accordingly, during the streak breakdown process, the time derivative of mode $M^*(0,\beta)$, i.e.

$$\mathcal{R}=\frac{\mathrm{d}M^*(0,\beta)}{\mathrm{d}t}, \tag{3.11}$$

becomes negative. An increase in the magnitude of negative-$\mathcal{R}$ indicates a more intense breakdown of the streaks.

Since the regeneration of streamwise vortices is primarily governed by the vortex stretching mechanism, we define a quantitative measure of vortex regeneration strength based on the modal interaction between streamwise vorticity and the streamwise velocity gradient (Jiménez & Moin 1991; Hamilton *et al.* 1995):

$$S(0,\beta)=\sum_{(p,q)\in\mathcal{I}}\int_0^{L_y}\widehat{\omega}_x(p\alpha,\,y,\,q\beta)\,\frac{\partial\widehat{u}(r\alpha,\,y,\,s\beta)}{\partial x}\mathrm{d}y, \tag{3.12}$$

where the set $\mathcal{I}$ includes the 12 mode pairs of $p=\pm1$ and $q\in\{-2,-1,0,1,2,3\}$, and the indices $r,s\in\mathbb{Z}$ satisfy $p+r=0$ and $q+s=1$. The modulus $|S(0,\beta)|$ represents the vortex-regeneration strength, and its normalised form is defined as $S^*(0,\beta)=\delta\,|S(0,\beta)|/U_b^2$.

Figure 13(*b*) compares the temporal evolution of key components of the self-sustaining cycle at $\Phi_m=0.512$ and 0.768, each with $\overline{St}^2_{el,<}=2.0$ and 2.2. In the turbulent regime, all components exhibit well-defined quasi-periodic behaviour, indicative of a sustained self-sustaining cycle. As the electrical effect intensifies, these quantities initially follow the turbulent trajectory but rapidly decay to zero, signalling relaminarisation. Notably, the suppression begins with streak breakdown (i.e. negative-$\mathcal{R}$), followed by the sequential decay of meandering streaks $M^*(\alpha,0)$, vortex regeneration $S^*(0,\beta)$, streamwise vortices $\Gamma^*(0,\beta)$, streak formation $\mathcal{L}^*(0,\beta)$, and finally the streaks themselves $M^*(0,\beta)$ (see figure 13*c*). This sequence reveals that streak breakdown is the most susceptible to disruption. Essentially, the electrical force alters the particle velocity and mass loading, and consequently the feedback force in (2.2) (see figure 7), thereby dismantling the self-sustaining cycle once a critical electrical Stokes number is exceeded.

A schematic diagram illustrating how electrical effects progressively suppress the subprocesses within the self-sustaining cycle is provided in figure 14. The suppression begins with the inhibition of streak breakdown, and eventually extends to large-scale streaks. Since the complete vanishing of streak breakdown occurs prior to the onset of attenuation of large-scale streaks, the feedback loop of the self-sustaining cycle is disrupted, thereby leading to relaminarisation of the flow.

At fixed Φ_m, a characteristic feature of wall drag modulation by electrical effects is the non-monotonic variation of C_f with increasing $\overline{St}^2_{el,<}$ in the turbulent regime, and a monotonic increase in the laminar regime. To elucidate this behaviour, we focus, without loss of generality, on representative cases with $\Phi_m=0.512$ and 0.768, and examine the relative contributions of viscous, Reynolds and particle stresses to C_f, as defined in (3.7). As shown in figure 15, the viscous stress contribution remains nearly constant

https://doi.org/10.1017/jfm.2025.10990 Published online by Cambridge University Press

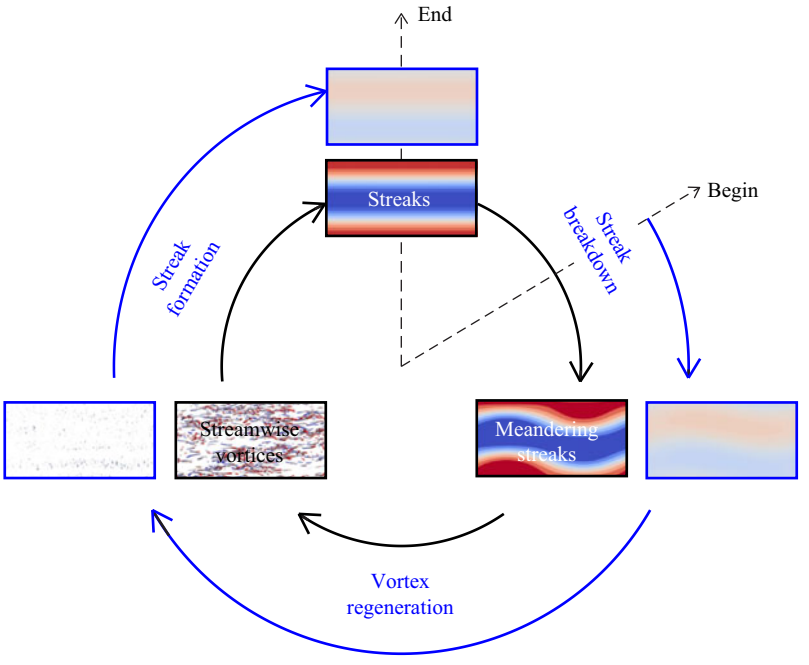


Figure 14. A schematic diagram of the physical mechanism underlying the relaminarisation induced by electrical effects. The inner black arrows depict the near-wall self-sustaining cycle in the turbulent regime, whereas the outer blue arrows illustrate the process by which electrical effects disrupt this cycle.

(~ 0.26) across all cases, as it is primarily confined to the viscous sublayer and is largely unaffected by particles. In contrast, the Reynolds stress contribution decreases monotonically with increasing $\overline{St}^2_{el,<}$, consistent with figure 3. Also, this decline arises from enhanced turbulence attenuation due to electrical effects (figure 9). The particle stress contribution, on the other hand, generally increases with $\overline{St}^2_{el,<}$, except for a slight drop at the onset of relaminarisation, where a sudden flow transition occurs (see vertical dashed lines in figure 15*b*,*d*). The opposing trends of decreasing Reynolds stress and increasing particle stress, together with the nearly constant viscous stress, give rise to the observed non-monotonic behaviour of C_f in the turbulent regime. In the laminar regime, however, the vanishing Reynolds stress and the monotonically increasing particle stress contribution lead to a sustained rise in C_f with increasing $\overline{St}^2_{el,<}$.

4. Conclusions

To conclude, we discover the role of electrical effects in particle-laden turbulent channel flows through 119 high-fidelity DNS. Electrical effects are shown to induce relaminarisation and substantially modify wall drag. The transition from turbulent to laminar flow is characterised by significant changes in the statistical behaviour of both the carrier fluid and dispersed particulate phases. Nevertheless, with increasing electrical effects, the wall-normal profiles of mean streamwise velocity and mean local particle mass loading exhibit distinctly different trends depending on the flow regime. In the turbulent regime, electrostatic drift-induced migration of smaller particles towards the wall is considerably suppressed, whereas turbophoretic migration of larger particles away from the wall becomes notably enhanced in the outer region. These combined processes lead to a reduction in particle accumulation near the wall, and an associated increase in the

https://doi.org/10.1017/jfm.2025.10990 Published online by Cambridge University Press

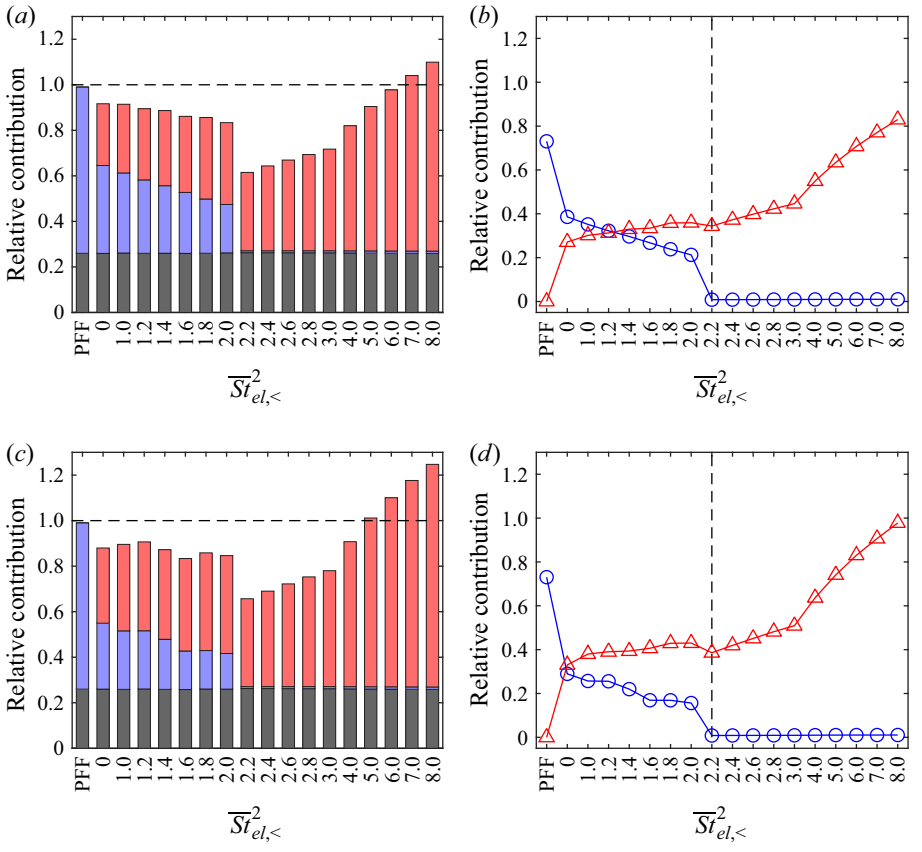


Figure 15. (*a*) Relative contributions of viscous (grey bars), Reynolds (blue bars) and particle (red bars) stresses to the wall friction coefficient C_f as a function of $\overline{St}^2_{el,<}$ at particle mass loading $\Phi_m = 0.512$, normalised by that of particle-free flow (PFF) C_{f0}. (*b*) Reynolds (blue circles) and particle (red triangles) stress contributions from (*a*), highlighting their evolution with $\overline{St}^2_{el,<}$. The vertical dashed line marks the threshold $\overline{St}^2_{el,<}$ for relaminarisation. (*c*,*d*) Same as (*a*,*b*) but for a higher particle loading $\Phi_m = 0.768$.

outer layer. Conversely, under laminar conditions, turbophoresis-driven migration away from the wall is substantially weakened for particles of all sizes, resulting in increased particle concentration near the wall, and decreased mass loading in the outer region.

Three distinct flow regimes emerge in the $(\Phi_m, \overline{St}^2_{el,<})$ parameter space: (I) a drag-reduced turbulent regime, (II) a drag-reduced laminar regime, and (III) a drag-enhanced laminar regime. The underlying mechanism is traced to the disruption of the self-sustaining cycle, wherein electrostatic forces first suppress streak breakdown, followed by sequential attenuation of meandering streaks, vortex regeneration, streamwise vortices and streak formation. This progressive suppression leads to relaminarisation under sufficiently strong coupling. In the turbulent regime, wall drag exhibits a non-monotonic dependence on $\overline{St}^2_{el,<}$, resulting from the competing effects of decreasing Reynolds stress and increasing particle stress, while viscous stress remains nearly constant. In contrast, under laminar regimes, the Reynolds stress vanishes, and the monotonic increase of particle stress with $\overline{St}^2_{el,<}$ leads to a consistent rise in wall friction. These findings highlight the critical role of electrical effects in modulating momentum transport, wall drag and flow-regime transitions in particle-laden turbulence.

https://doi.org/10.1017/jfm.2025.10990 Published online by Cambridge University Press

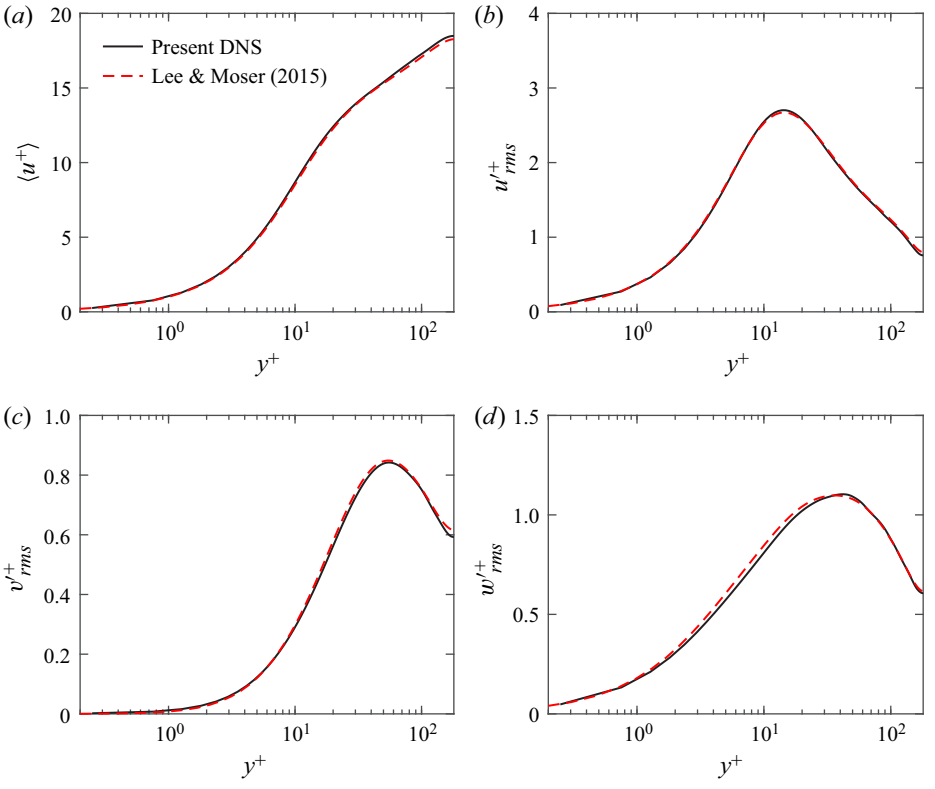


Figure 16. Wall-normal profiles of (*a*) the mean streamwise fluid velocity, (*b*) the r.m.s. streamwise fluid velocity fluctuation, (*c*) the r.m.s. wall-normal fluid velocity fluctuation, and (*d*) the r.m.s. spanwise fluid velocity fluctuation. The solid black lines indicate the present DNS results, while the dashed red lines correspond to the data of Lee & Moser (2015).

Acknowledgements. Y.C. and X.T. contributed equally to this work and should be considered co-first authors.

Funding. This study was supported by the National Natural Science Foundation of China (grant nos 12388101, 12472252, 123B2033) and the Fundamental Research Funds for the Central Universities (grant no. lzujbky-2025-ytA04).

Declaration of interests. The authors report no conflict of interests.

Appendix. Validation of the Eulerian–Lagrangian computational framework

To assess the accuracy of the present numerical simulations, particle-free turbulent channel flow results at $Re_\tau = 180$ are compared against the DNS dataset of Lee & Moser (2015) at the same Reynolds number (see figure 16). The agreement is excellent for all velocity statistics, with the largest discrepancy in the r.m.s. spanwise velocity fluctuation, being within 3.4 %. Such a minor deviation is likely attributable to differences in the computational grid. To further verify the accuracy of particle trajectory integration, benchmark simulations of three particle Stokes numbers ($St^+ = 1$, 5 and 25) at $Re_\tau = 150$ are reproduced based on the DNS dataset of Marchioli *et al.* (2008). As shown in figure 17, the present results are in close agreement with the reference data. Notably, the present simulations employ a finer grid resolution ($N_x \times N_y \times N_z = 192 \times 192 \times 192$) compared to $128 \times 129 \times 128$ in Marchioli *et al.* (2008), which results in smoother and more stable

https://doi.org/10.1017/jfm.2025.10990 Published online by Cambridge University Press

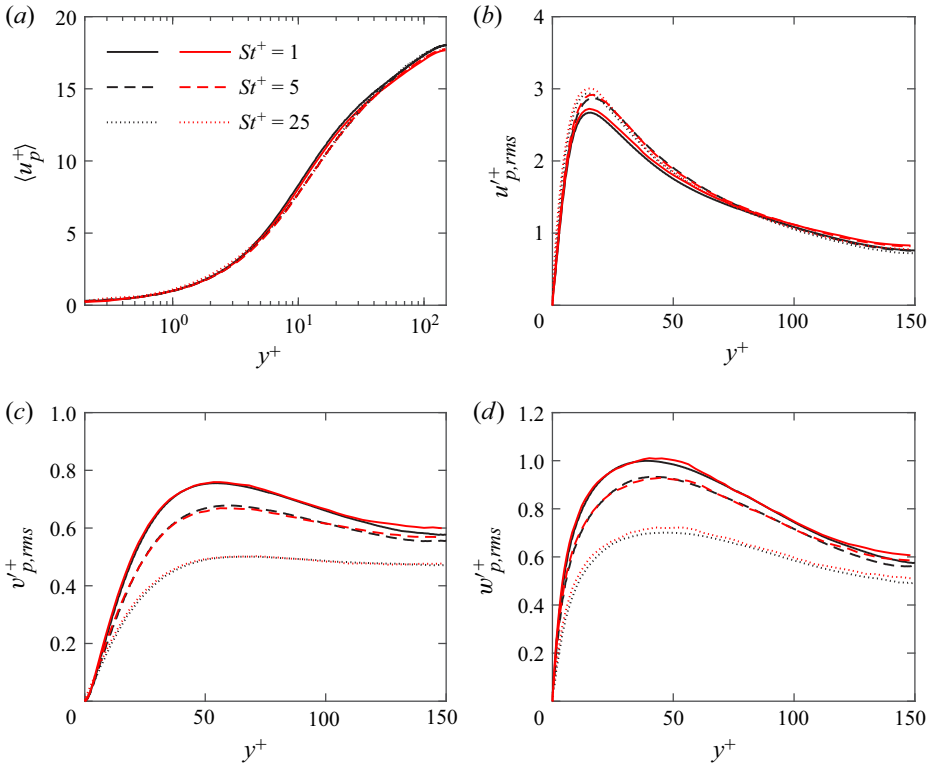


Figure 17. Wall-normal profiles of (*a*) the mean streamwise particle velocity, (*b*) the r.m.s. streamwise particle velocity fluctuation, (*c*) the r.m.s. wall-normal particle velocity fluctuation, and (*d*) the r.m.s. spanwise particle velocity fluctuation. The black lines indicate the present DNS results, while the red lines correspond to the data of Marchioli *et al.* (2008).

profiles. These two comparisons jointly provide compelling evidence for the fidelity and robustness of the present particle-laden flow solver.

References

Alipchenkov, V.M., Zaichik, L.I. & Petrov, O.F. 2004 Clustering of charged particles in isotropic turbulence. *High Temp.* **42**, 919–927.

Baddeley, P.F.H. 1860 *Whirlwinds and Dust-Storms of India*. Bell & Daldy.

Bakewell, H.P.Jr & Lumley, J.L. 1967 Viscous sublayer and adjacent wall region in turbulent pipe flow. *Phys. Fluids* **10**, 1880–1889.

Balachandar, S. & Eaton, J.K. 2010 Turbulent dispersed multiphase flow. *Annu. Rev. Fluid Mech.* **42**, 111–133.

Bec, J., Gustavsson, K. & Mehlig, B. 2024 Statistical models for the dynamics of heavy particles in turbulence. *Annu. Rev. Fluid Mech.* **56**, 189–213.

Boivin, M., Simonin, O. & Squires, K.D. 1998 Direct numerical simulation of turbulence modulation by particles in isotropic turbulence. *J. Fluid Mech.* **375**, 235–263.

Boutsikakis, A., Fede, P. & Simonin, O. 2022 Effect of electrostatic forces on the dispersion of like-charged solid particles transported by homogeneous isotropic turbulence. *J. Fluid Mech.* **938**, A33.

Brandt, L. & Coletti, F. 2022 Particle-laden turbulence: progress and perspectives. *Annu. Rev. Fluid Mech.* **54**, 159–189.

Cimarelli, C., Alatorre-Ibargüengoitia, M.A., Kueppers, U., Scheu, B. & Dingwell, D.B. 2014 Experimental generation of volcanic lightning. *Geology* **42**, 79–82.

Costa, P. 2018 A FFT-based finite-difference solver for massively-parallel direct numerical simulations of turbulent flows. *Comput. Maths Appl.* **76**, 1853–1862.

Cranfield, R.H. 1929 Atmospheric electricity during sand storms. *Science* **69**, 474–475.

https://doi.org/10.1017/jfm.2025.10990 Published online by Cambridge University Press

CROZIER, W.D. 1964 The electric field of a New Mexico dust devil. *J. Geophys. Res.* **69**, 5427–5429.
CUI, Y., ZHANG, H. & ZHENG, X. 2024 Turbulence modulation by charged inertial particles in channel flow. *J. Fluid Mech.* **990**, A2.
EATON, J.K. & FESSLER, J. 1994 Preferential concentration of particles by turbulence. *Intl J. Multiphase Flow* **20**, 169–209.
ELLINGSEN, T. & PALM, E. 1975 Stability of linear flow. *Phys. Fluids* **18**, 487–488.
ESPOSITO, F., *et al.* 2016 The role of the atmospheric electric field in the dust-lifting process. *Geophys. Res. Lett.* **43**, 5501–5508.
FARRELL, W.M., KAISER, M.L., DESCH, M.D., HOUSER, J.G., CUMMER, S.A., WILT, D.M. & LANDIS, G.A. 1999 Detecting electrical activity from Martian dust storms. *J. Geophys. Res. Planets* **104**, 3795–3801.
FERRANTE, A. & ELGHOBASHI, S. 2003 On the physical mechanisms of two-way coupling in particle-laden isotropic turbulence. *Phys. Fluids* **15**, 315–329.
FORWARD, K.M., LACKS, D.J. & SANKARAN, R.M. 2009 Charge segregation depends on particle size in triboelectrically charged granular materials. *Phys. Rev. Lett.* **102**, 028001.
FREIER, G.D. 1960 The electric field of a large dust devil. *J. Geophys. Res.* **65**, 3504.
FUKAGATA, K., IWAMOTO, K. & KASAGI, N. 2002 Contribution of Reynolds stress distribution to the skin friction in wall-bounded flows. *Phys. Fluids* **14**, L73–L76.
GAO, W., SAMTANEY, R. & RICHTER, D.H. 2023 Direct numerical simulation of particle-laden flow in an open channel at $Re_\tau = 5186$. *J. Fluid Mech.* **957**, A3.
GILBERT, J.S., LANE, S.J., SPARKS, R.S.J. & KOYAGUCHI, T. 1991 Charge measurements on particle fallout from a volcanic plume. *Nature* **349**, 598–600.
GROSSHANS, H. & PAPALEXANDRIS, M.V. 2017 Direct numerical simulation of triboelectric charging in particle-laden turbulent channel flows. *J. Fluid Mech.* **818**, 465–491.
HAMILTON, J.M. & ABERNATHY, F.H. 1994 Streamwise vortices and transition to turbulence. *J. Fluid Mech.* **264**, 185–212.
HAMILTON, J.M., KIM, J. & WALEFFE, F. 1995 Regeneration mechanisms of near-wall turbulence structures. *J. Fluid Mech.* **287**, 317–348.
HARRIS, D.J. 1967 Electrical effects of the Harmattan dust storms. *Nature* **214**, 585–585.
HARRISON, R.G., *et al.* 2016 Applications of electrified dust and dust devil electrodynamics to Martian atmospheric electricity. *Space Sci. Rev.* **203**, 299–345.
HOUGHTON, I.M.P., APLIN, K.L. & NICOLL, K.A. 2013 Triboelectric charging of volcanic ash from the 2011 Grímsvötn eruption. *Phys. Rev. Lett.* **111**, 118501.
HWANG, Y. & COSSU, C. 2010 Self-sustained process at large scales in turbulent channel flow. *Phys. Rev. Lett.* **105**, 044505.
JANTAČ, S. & GROSSHANS, H. 2024 Suppression and control of bipolar powder charging by turbulence. *Phys. Rev. Lett.* **132**, 054004.
JIMÉNEZ, J. & MOIN, P. 1991 The minimal flow unit in near-wall turbulence. *J. Fluid Mech.* **225**, 213–240.
JIMÉNEZ, J. & PINELLI, A. 1999 The autonomous cycle of near-wall turbulence. *J. Fluid Mech.* **389**, 335–359.
JOHNSON, P.L., BASSENNE, M. & MOIN, P. 2020 Turbophoresis of small inertial particles: theoretical considerations and application to wall-modelled large-eddy simulations. *J. Fluid Mech.* **883**, A27.
KAMRA, A.K. 1972 Physical sciences: visual observation of electric sparks on gypsum dunes. *Nature* **240**, 143–144.
KIM, J. & MOIN, P. 1985 Application of a fractional-step method to incompressible Navier–Stokes equations. *J. Comput. Phys.* **59**, 308–323.
KOK, J.F. & RENNO, N.O. 2006 Enhancement of the emission of mineral dust aerosols by electric forces. *Geophys. Res. Lett.* **33**, L19S10.
KOK, J.F. & RENNO, N.O. 2008 Electrostatics in wind-blown sand. *Phys. Rev. Lett.* **100**, 014501.
KOLEHMAINEN, J., OZEL, A., BOYCE, C.M. & SUNDARESAN, S. 2016 A hybrid approach to computing electrostatic forces in fluidized beds of charged particles. *AIChE J.* **62** (7), 2282–2295.
LEE, M. & MOSER, R.D. 2015 Direct numerical simulation of turbulent channel flow up to $Re_\tau \approx 5200$. *J. Fluid Mech.* **774**, 395–415.
LOZANO-DURÁN, A., BAE, H.J. & ENCINAR, M.P. 2020 Causality of energy-containing eddies in wall turbulence. *J. Fluid Mech.* **882**, A2.
LU, J., NORDSIEK, H., SAW, E.W. & SHAW, R.A. 2010 Clustering of charged inertial particles in turbulence. *Phys. Rev. Lett.* **104**, 184505.
MARCHIOLI, C., SOLDATI, A., KUERTEN, J.G.M., ARCEN, B., TANIERE, A., GOLDENSOPH, G., SQUIRES, K.D., CARGNELUTTI, M.F. & PORTELA, L.M. 2008 Statistics of particle dispersion in direct numerical

https://doi.org/10.1017/jfm.2025.10990 Published online by Cambridge University Press

simulations of wall-bounded turbulence: results of an international collaborative benchmark test. *Intl J. Multiphase Flow* **34**, 879–893.
MAXEY, M.R. 1987 The gravitational settling of aerosol particles in homogeneous turbulence and random flow fields. *J. Fluid Mech.* **174**, 441–465.
MAXEY, M.R. & RILEY, J.J. 1983 Equation of motion for a small rigid sphere in a nonuniform flow. *Phys. Fluids* **26**, 883–889.
MÉNDEZ HARPER, J.S., MCDONALD, G.D., DUFEK, J., MALASKA, M.J., BURR, D.M., HAYES, A.G., MCADAMS, J. & WRAY, J.J. 2017 Electrification of sand on Titan and its influence on sediment transport. *Nat. Geosci.* **10**, 260–265.
MOTOORI, Y. & GOTO, S. 2025 Attenuation mechanism of wall-bounded turbulence by heavy finite-size particles. *J. Fluid Mech.* **1014**, A30.
MOTOORI, Y., WONG, C. & GOTO, S. 2022 Role of the hierarchy of coherent structures in the transport of heavy small particles in turbulent channel flow. *J. Fluid Mech.* **942**, A3.
OWEN, P.R. 1969 Pneumatic transport. *J. Fluid Mech.* **39**, 407–432.
POELMA, C. & OOMS, G. 2006 Particle–turbulence interaction in a homogeneous, isotropic turbulent suspension. *ASME Appl. Mech. Rev.* **59**, 78–90.
POPE, S.B. 2000 *Turbulent Flows*. Cambridge University Press.
RAHMAN, M.M., SAIEED, A. & HICKEY, J.P. 2023 Turbulence-induced electrical discharges in charged particle-laden Martian boundary layers. *Flow* **3**, E34.
REDDY, S.C., SCHMID, P.J., BAGGETT, J.S. & HENNINGSON, D.S. 1998 On stability of streamwise streaks and transition thresholds in plane channel flows. *J. Fluid Mech.* **365**, 269–303.
RICHTER, D.H. & SULLIVAN, P.P. 2013 Momentum transfer in a turbulent, particle-laden Couette flow. *Phys. Fluids* **25**, 055103.
RUAN, X., DIAZ-LOPEZ, M.X., GORMAN, M.T. & NI, R. 2025 Direct numerical simulations on transport and deposition of charged inertial particles in turbulent channel flow. *J. Fluid Mech.* **1010**, A49.
RUAN, X., GORMAN, M.T. & NI, R. 2024 Effects of electrostatic interaction on clustering and collision of bidispersed inertial particles in homogeneous and isotropic turbulence. *J. Fluid Mech.* **980**, A29.
RUDGE, W.A.D. 1913 Atmospheric electrification during South African dust storms. *Nature* **91**, 31–32.
SCHILLER, L. & NAUMANN, A. 1935 A drag coefficient correlation. *Z. Verein. Deutsch. Ing.* **77**, 318–320.
SCHMIDT, D.S., SCHMIDT, R.A. & DENT, J.D. 1998 Electrostatic force on saltating sand. *J. Geophys. Res.: Atmos.* **103**, 8997–9001.
SCHMIDT, D.S., SCHMIDT, R.A. & DENT, J.D. 1999 Electrostatic force in blowing snow. *Boundary-Layer Meteorol.* **93**, 29–45.
SHINBROT, T. & HERRMANN, H.J. 2008 Static in motion. *Nature* **451**, 773–774.
SIPPOLA, P., KOLEHMAINEN, J., OZEL, A., LIU, X., SAARENRINNE, P. & SUNDARESAN, S. 2018 Experimental and numerical study of wall layer development in a tribocharged fluidized bed. *J. Fluid Mech.* **849**, 860–884.
SQUIRES, K.D. & EATON, J.K. 1990 Particle response and turbulence modification in isotropic turbulence. *Phys. Fluids* **2**, 1191–1203.
STOW, C.D. 1969 Dust and sand storm electrification. *Weather* **24**, 134–144.
SUNDARAM, S. & COLLINS, L.R. 1999 A numerical study of the modulation of isotropic turbulence by suspended particles. *J. Fluid Mech.* **379**, 105–143.
VREMAN, A. 2015 Turbulence attenuation in particle-laden flow in smooth and rough channels. *J. Fluid Mech.* **773**, 103–136.
WALEFFE, F. 1997 On a self-sustaining process in shear flows. *Phys. Fluids* **9**, 883–900.
WANG, G. & RICHTER, D.H. 2019 Modulation of the turbulence regeneration cycle by inertial particles in planar Couette flow. *J. Fluid Mech.* **861**, 901–929.
XIA, Y., YU, Z., LIN, Z. & GUO, Y. 2022 Improved modelling of interfacial terms in the second-moment closure for particle-laden flows based on interface-resolved simulation data. *J. Fluid Mech.* **952**, A25.
XU, A., XU, B.R. & XI, H.D. 2024 Particle transport and deposition in wall-sheared thermal turbulence. *J. Fluid Mech.* **999**, A15.
YU, Z., LIN, Z., SHAO, X. & WANG, L.P. 2017 Effects of particle–fluid density ratio on the interactions between the turbulent channel flow and finite-size particles. *Phys. Rev. E* **96**, 033102.
YU, Z., XIA, Y., GUO, Y. & LIN, J. 2021 Modulation of turbulence intensity by heavy finite-size particles in upward channel flow. *J. Fluid Mech.* **913**, A3.
ZHANG, H., CUI, Y. & ZHENG, X. 2023 How electrostatic forces affect particle behaviour in turbulent channel flows. *J. Fluid Mech.* **967**, A8.
ZHANG, H. 2024 Structure and coupling characteristics of multiple fields in dust storms. *Acta Mech. Sin.* **40**, 123339.

https://doi.org/10.1017/jfm.2025.10990 Published online by Cambridge University Press

ZHANG, H., TAN, X. & ZHENG, X. 2023 Multifield intermittency of dust storm turbulence in the atmospheric surface layer. *J. Fluid Mech.* **963**, A15.
ZHANG, H. & ZHENG, X. 2025 Wavelet analysis of the coupling between turbulence, particles and electrostatics in dust storms. *J. Fluid Mech.* **1007**, A8.
ZHANG, H. & ZHOU, Y.H. 2020 Reconstructing the electrical structure of dust storms from locally observed electric field data. *Nat. Commun.* **11**, 5072.
ZHANG, H. & ZHOU, Y.H. 2023 Unveiling the spectrum of electrohydrodynamic turbulence in dust storms. *Nat. Commun.* **14**, 408.
ZHAO, L., ANDERSSON, H.I. & GILLISSEN, J.J. 2013 Interphasial energy transfer and particle dissipation in particle-laden wall turbulence. *J. Fluid Mech.* **715**, 32–59.
ZHAO, Y., LIU, M., LI, J., YAN, Y. & YAO, J. 2022 Modulation of turbulence by dispersed charged particles in pipe flow. *Phys. Fluids* **34**, 123315.
ZHENG, X. 2009 *Mechanics of Wind-Blown Sand Movements*. Springer Science & Business Media.
ZHENG, X., FENG, S. & WANG, P. 2021 Modulation of turbulence by saltating particles on erodible bed surface. *J. Fluid Mech.* **918**, A16.
ZHENG, X.J. 2013 Electrification of wind-blown sand: recent advances and key issues. *Eur. Phys. J. E* **36**, 138.
ZHENG, X.J., HUANG, N. & ZHOU, Y.H. 2003 Laboratory measurement of electrification of wind-blown sands and simulation of its effect on sand saltation movement. *J. Geophys. Res.: Atmos.* **108**, 4322.
ZHENG, X.J., HUANG, N. & ZHOU, Y.H. 2006 The effect of electrostatic force on the evolution of sand saltation cloud. *Eur. Phys. J. E* **19**, 129–138.

https://doi.org/10.1017/jfm.2025.10990 Published online by Cambridge University Press